

Measuring the size of non-spherical particles and the implications for grain size analysis in volcanology



Hannah M. Buckland ^{a,*}, Jennifer Saxby ^b, Matt Roche ^a, Phoebe Meredith ^a, Alison C. Rust ^a, Katharine V. Cashman ^a, Samantha L. Engwell ^c

^a School of Earth Sciences, University of Bristol, Wills Memorial Building, Bristol, UK

^b School of Earth and Environment, University of Leeds, Leeds, UK

^c British Geological Survey, The Lyell Centre, Edinburgh, UK

ARTICLE INFO

Article history:

Received 22 January 2021

Received in revised form 16 April 2021

Accepted 21 April 2021

Available online 24 April 2021

Keywords:

Tephra

Volcanic ash

Particle size

Particle shape

Image analysis

Dispersion modelling

ABSTRACT

To quantify the size of tephra, two practical challenges must be addressed: the wide range of particle sizes (10^{-8} - 10^1 m) and the diversity of particle shape, density and optical properties. Here we use dynamic image analysis (DIA) to simultaneously characterise the size and shape of tephra samples from Mount Mazama, Krafla, Mount St. Helens and Campi Flegrei. The Camsizer X2 instrument used in this study, which has a measurement range of 0.8 μm - 8 mm, avoids the need to overlap different measurement methods and principles for fine (<125 μm) and coarse (>125 μm) particle sizes. Importantly, DIA does not require an assumption of particle properties. DIA also allows the measurement of grain size distributions (GSDs) using multiple size definitions. Quantification by particle long axis and the area equivalent sphere diameter, for example, make DIA GSDs compatible with the outputs of other methods such as laser diffraction and sieving. Parallel mass-based (sieving) and volume-based (DIA) GSDs highlight the effects of particle density variations on methods of size analysis; concentrations of dense crystals within a narrow size range, in particular, can affect mass-based GSDs and their interpretations. We also show that particle shape has an important effect on the apparent grain size of distal tephra. Extreme particle shapes, such as the platy glass shards typical of the distal Campanian Ignimbrite deposits, can appear coarser than other distal tephras if size is quantified according to the particle long axis. These results have important implications for ash dispersion models, where input GSDs assume that reported measurements are for volume-equivalent sphere diameters. We conclude that DIA methods are not only suitable for characterising, simultaneously, the size and shape of ash particles but also provide new insights into particle properties that are useful for both ash dispersion modelling and studies of explosive volcanism.

© 2021 Published by Elsevier B.V.

1. Introduction

Particles with highly irregular shapes, such as the products of explosive volcanic eruptions (tephra), present a particular challenge when quantifying particle size. The 'size' of non-spherical particles can be quantified in multiple ways depending on the method of measurement and definition of 'size'. For example, size can be measured as the longest particle dimension using callipers, or the diameter of a volume equivalent sphere calculated from 3D data (Bagheri et al., 2015; Saxby et al., 2020). A clear and consistent definition of size is important because the 'size' of tephra is used to predict the dispersal of the particles in the atmosphere (Rose and Durant, 2009; Mele et al., 2011; Engwell and Eychenne, 2016; Saxby et al., 2018). The Grain Size Distribution (GSD) of tephra also provides insight into fragmentation mechanisms (e.g., Barberi et al., 1989; Wohletz et al., 1989; Jones et al., 2016; Mele

et al., 2020) and estimates of eruption column heights for unobserved eruptions (e.g., Carey and Sparks, 1986; Burden et al., 2011; Rossi et al., 2019). Additionally, accurate measurements of the GSD of volcanic ash (tephra <2 mm) are important for understanding the risks posed to human health and infrastructure (Horwell and Baxter, 2006; Horwell, 2007; Bebbington et al., 2008; Wilson et al., 2012; Blake et al., 2017) and the efficiency of wind-driven remobilisation (Hadley et al., 2004; Leadbetter et al., 2012; Liu et al., 2014; Panebianco et al., 2017). Finally, quantitative measurements of particle shape complement size analysis and are equally important for interpreting eruptive processes and forecasting tephra transport and sedimentation (Heiken, 1972; Riley et al., 2003; Cioni et al., 2014; Bagheri et al., 2015; Liu et al., 2015; Saxby et al., 2018; Dürig et al., 2020).

One of the main challenges faced when characterising a tephra deposit is the large range of particle sizes produced by an eruption (from 10^{-8} - 10^1 m). This has required the use of a variety of methods to measure size, often requiring an overlap of two or more methods to analyse the coarse and fine components of a single sample. Numerous size and

* Corresponding author.

E-mail address: hannah.buckland@bristol.ac.uk (H.M. Buckland).

shape parameters are associated with different methods and the choice of parameter has implications for data interpretation and comparison. Furthermore, particle size and shape are typically analysed separately using different methods, leading to slow data collection and processing as noted by several authors who have investigated the range of shape parameters and size characterisation methods for volcanic ash (Riley et al., 2003; Leibrandt and Le Pennec, 2015; Liu et al., 2015). Thus, despite the importance of grain size and shape characterisation, data compilation and comparison across different studies is hindered by the range of methods used.

Tephra from a single eruption is a mixture of components (e.g., lithics, free-crystals and juvenile fragments such as pumice) and each component can have unique optical and physical properties (e.g., refractive index, density, porosity and permeability) which can limit the efficacy of grain size methods initially developed for analysing more homogeneous materials. The different components within a single sample can have individual GSDs that overlap to produce the GSD of the whole sample (Moore, 1934; Walker, 1971; Sparks, 1976; Mele et al., 2020). A further complication is that the relative proportion of each component can vary spatially in a deposit due to emplacement and transport processes (Sparks and Walker, 1977; Carey and Sigurdsson, 1982; Williams and Self, 1983; Eychenne et al., 2015). For example, crystal concentrations observed in fall deposits reflect a narrow crystal size and density distribution that causes deposition over a limited transport distance. Grain size procedures that do not account for variations in particle density or componentry with size (e.g., sieving) could therefore produce inaccurate interpretations of GSDs.

Here we outline an analytical protocol for simultaneous size and shape characterisation using a fast and flexible method that employs dynamic image analysis (DIA). Methods of size measurement that use image analysis do not need to assume particle shape, which is analysed simultaneously. Imaging individual particles also means that multiple size parameters (e.g., particle long axis and equivalent circle diameter) are measured concurrently. This provides both adaptability and consistency when reporting size measurements. First, we discuss the significance of grain size measurement in studies of explosive volcanism (Section 2) and review grain size analysis methods with emphasis on how 'size' is quantified (Table 1; Appendix A). We then outline a methodology for size analysis using DIA with example analyses using spherical and non-spherical particles (Section 3). We follow this by discussing

the benefits of DIA for measuring the grain size of tephra and examine the implications of using different size measurements in volcanological applications (Sections 4–5). We conclude by showing ways in which inconsistencies in size definitions for non-spherical particles affect studies of explosive volcanism, particularly when particle shapes are extreme, as is common for glass shards.

2. Background

Analysing the grain size of tephra is a long-established practise in volcanology and the standard methodologies applied were adopted from the wider field of sedimentology (Wentworth, 1922; Krumbein, 1934; Pettijohn, 1949). For example, early work characterising the grain size of field deposits helped distinguish poorly sorted pyroclastic density current deposits (nuée ardente or ignimbrite deposits) from well sorted airfall deposits (Lacroix, 1904; Moore, 1934; Fenner, 1937). Standard statistical procedures from sedimentology were also adopted, such as characterising GSDs using the maximum clast size, median diameter (M_d) and sorting (σ ; Fisher, 1964). Also adapted from sedimentology is the practise of deconvolving multi-modal GSDs into sub-populations. Studies of sands attribute sub-populations in multi-modal GSDs to the genesis of the material (Visher, 1969) and when applied to volcanic GSDs, grain size sub-populations can be related to eruptive processes (Sheridan, 1971; Wohletz et al., 1989; Engwell et al., 2014; Eychenne et al., 2015). Whilst these procedures have merit and can provide insight into volcanic processes, the complex and heterogeneous physical properties of tephra as a result of the mixture of components suggests that volcanic GSDs measured using traditional grain size methods may need additional scrutiny.

2.1. Why is grain size important for volcanology?

Grain size data are used to interpret two key eruption source parameters (ESPs), the eruption column height (Carey and Sparks, 1986; Woods and Wohletz, 1991; Sparks et al., 1992; Burden et al., 2011) and the total grain size distribution (TGSD; Carey and Sigurdsson, 1982; Bonadonna and Houghton, 2005). Both parameters are used to interpret the nature of eruptive activity from field deposits. Eruption column height can be inferred from modelled clast support envelopes within the eruption column (Carey and Sparks, 1986) and requires

Table 1

Summary of grain size methods discussed in this study with measurement range and the assumptions required to quantify size.

Method name	Measurement range (μm)	Method assumptions	Size measure	Mass or volume distribution
Sieving	20–125,000	Sieve aperture only equal to particle size if spherical	Diameter for spheres, minimum to intermediate dimension for non-spherical particles	M
Pipette method	50–5000	Constant density spheres	Equivalent settling velocity sphere diameter	V
Roller apparatus	1–100	Settling velocity classes of constant density spheres	Equivalent settling velocity sphere diameter	V
Laser diffraction (Mie theory)	0.01–3500	Spherical particles, constant refractive index	Volume equivalent sphere diameter	V
Laser diffraction (Fraunhofer approximation)	10–3500 μm	Flat disc particles, particles only cause diffraction	Maximum width	V
Electrozone sensing (e.g., Coulter counter)	0.4–1600	Spherical particles	Volume equivalent sphere diameter	V
Image analysis (SEM)	~0.01–200	Conversion from 2D area to 3D volume	2D Miscellaneous	V
Image analysis (Morphologi)	0.5–1300	Conversion from 2D area to 3D volume	2D Miscellaneous	V
Image analysis (cryptotephra)	20–250	Conversion from 2D area to 3D volume, material $<20 \mu\text{m}$ removed	2D Miscellaneous	V
Radar disdrometer (e.g., PLUDIX)	1000–10,000	Dense spherical particles	Volume equivalent sphere diameter	V
Laser disdrometer (e.g., Parsivel2)	200–25,000	Dense spherical particles	Volume equivalent sphere diameter or maximum width	V
High resolution video	62–2000	Conversion from 2D area to 3D volume	2D Miscellaneous	V
Satellite infrared retrievals	~0–100	Spherical particles, constant refractive index	Volume equivalent sphere diameter	V
Dynamic image analysis (e.g., Camsizer X2)	0.8–8000	Conversion from 2D area to 3D volume	2D Miscellaneous	V

maximum clast size data that are typically measured in the field on a sub-sample of the largest clasts (Bonadonna et al., 2013). TGSDs are produced by combining GSDs from multiple sampling sites across the tephra deposit and weighting them according to the mass accumulation of tephra (Carey and Sigurdsson, 1982; Bonadonna and Houghton, 2005).

ESPs are a key requirement for ash dispersion models, which can be used to reconstruct past eruptions or to forecast tephra dispersal from future eruptions (Mastin et al., 2009; Webley et al., 2009; Bonadonna et al., 2012; Beckett et al., 2015). Most operational and research-based ash dispersion models use an input particle size distribution (PSD), where PSD is used in reference to tephra in the atmosphere (Mastin et al., 2009; Bonadonna et al., 2012; Beckett et al., 2015; WMO, 2018). TGSDs determined from tephra deposits (on the ground) can be used to inform PSDs but there are several challenges to relating the two measures. First, TGSD estimates are sensitive to both the spatial coverage and number of individual GSDs measured (Bonadonna and Houghton, 2005; Alfano et al., 2016; Pioli et al., 2019), which can propagate as uncertainty in the outputs of dispersion models if TGSDs are used as input PSDs (Beckett et al., 2015). Second, most ash dispersion model PSDs describe a distribution of spherical particles (or particles with a fixed shape factor; Beckett et al., 2015; Saxby et al., 2018). Therefore, equating measured TGSDs directly to PSDs is not appropriate where particle shapes are not constant and 'size' measurements vary with particle shape and/or other physical properties such as density or refractive index.

An alternative to using TGSDs for ash dispersion modelling is to use PSDs that have been measured in situ from an active plume. In situ PSDs have been measured following aircraft encounters with ash clouds (Hobbs et al., 1991; Casadevall, 1994; Pieri et al., 2002), by flying sampling devices through plumes (e.g., Johnson et al., 2012; Petäjä et al., 2012; Mori et al., 2016; Schellenberg et al., 2019), from satellite retrievals (e.g., Prata and Grant, 2001; Bonadonna et al., 2011; Pavolonis et al., 2013; Gouhier et al., 2019) and using ground based sensors (Scollo et al., 2005; Bonadonna et al., 2011; Kozono et al., 2019). However, in situ measurements are limited to a small number of modern eruptions and the range of grain sizes is never fully covered by one technique. Furthermore, how 'size' is quantified is not consistent across ground-based or in situ techniques, which makes the combination and comparison of in situ PSDs and GSDs challenging (Bonadonna et al., 2011; Stevenson et al., 2015).

2.2. Grain size methods in volcanology

A wide variety of methods are used to quantify the size of tephra, including laboratory-based protocols such as sieve analysis, laser diffraction, electrozone sensing, particle sedimentation and image analysis, and in situ methods such as ground-based radar and satellite remote sensing (see Appendix 1 for details). Importantly, each method of size analysis measures the size of non-spherical particles according to a different definition of 'size' and several methods require an assumption or simplification of particle properties such as shape, density and refractive index (Appendix A; Table 1). For example, sieve analysis sorts irregular particles by both size and shape (Komar and Cui, 1984); GSDs measured by sieving, however, are reported as the mass fraction within grain size or sieve increments with no consideration of which particle dimension the sieve aperture refers to. Similarly, laser diffraction and electrozone sensing methods require an assumption of particle shape that allows the resulting GSDs to be quantified according to different particle dimensions (Table 1; Appendix 1). Quantifying grain size using image analysis can ensure consistency in the size parameter measured and simultaneous shape quantification. However, some image analysis methods require pre-analysis sample preparation, such as sieving, and substantial analysis time (~hours to days) to collect and process the images, particularly when fine material necessitates high resolution

images. For this reason, these methods can be time-consuming or burdensome when analysing large sample suites (>10's samples).

After measurement the convention is to report GSD statistics that facilitate comparison with other distributions. The most common parameters reported for volcanic GSDs are based on the Inman (1952) or Folk and Ward (1957) graphical methods which determine the mean (μ), median (Md), standard deviation or sorting (σ), skewness (Sk) and Kurtosis (K; Blott and Pye, 2001). These methods were designed for grain size data on the φ -scale and require very little data manipulation (Appendix B). This method, however, assumes that the GSD follows a log-normal distribution, in other words the GSD is normally distributed on the φ -scale. Alternatively, the GSD can be described using a Weibull or Rosin-Rammler distribution (Rosin and Rammler, 1933; Weibull, 1951; Brown and Wohletz, 1995) from which shape and scale parameters can be described (Appendix B). Log-normal and Weibull distributions can be fit as mixture models to account for the multimodal form of many volcanic GSDs (Appendix B; Eychenne et al., 2012, 2015; Costa et al., 2016; Pioli et al., 2019; Mele et al., 2020). The number and proportion of subpopulations provide additional parameters that can be compared between different samples; in some cases subpopulations can be related to distinct eruptive processes (e.g., Sheridan, 1971; Eychenne et al., 2012, 2015; Engwell et al., 2014).

Common themes found when reviewing grain size methodologies (Appendix A; Table 1) are the lack of quantified shape characterisation, the need to assume particle properties such as density and refractive index (sieving, sedimentation, laser diffraction and electrozone sensing), and the requirement of pre-analysis sample preparation (image analysis methods). Furthermore, the amount of material analysed varies between methods. Notably, methods and instruments commonly used in volcanology such as the Mastersizer 3000, Morphologi G3 and SEM image analysis use <10 mg of material per analysis, which can cause undercounting of large grains. Hence the rationale for developing approaches to particle size analysis that do not require assumptions of shape and the pertinence of methods that can measure multiple size parameters for non-spherical particles.

3. Methods

3.1. Instrumentation

Here we present a relatively new analytical approach to characterise the size and shape of tephra which addresses some of the limitations of other techniques. The protocol involves the CAMSIZER® X2 (CX2), a particle analyser manufactured by Microtrac MRB (formerly Retsch Technology) that utilises dynamic image analysis (DIA; ISO 13322-2) to characterise the grain size of particulate materials. Castro and Andronico (2008) published a detailed INGV report outlining similar procedures using an earlier CAMSIZER model, although the CX2 model described in this study has capabilities to work with much finer material ($>0.8 \mu\text{m}$) thanks to the multiple particle dispersion modules.

3.1.1. Basic functions of the CX2

The CX2 is a compact particle analyser that consists of three key components: the sample feeder and particle dispersal module, the imaging module, and a desktop computer running the CX2 software (Fig. 1). The DIA principle requires that particles are dispersed past the field of view of two high resolution digital cameras to image the moving particles that are back lit by an LED (Fig. 1). The combination of two cameras (one basic and one zoom) ensures that a range of particle sizes ($0.8 \mu\text{m} - 8 \text{ mm}$) can be imaged at an optimum resolution. These images are processed in real-time by the CX2 software to generate shape and size distributions and compute grain size statistics.

The particles are dispersed past the cameras' field of view by one of three mechanisms: wet dispersion (X-flow), compressed air (X-jet) or as free-falling particles (X-fall). Each dispersion mechanism has an optimum grain size range. The X-fall dispersion is best for coarse material

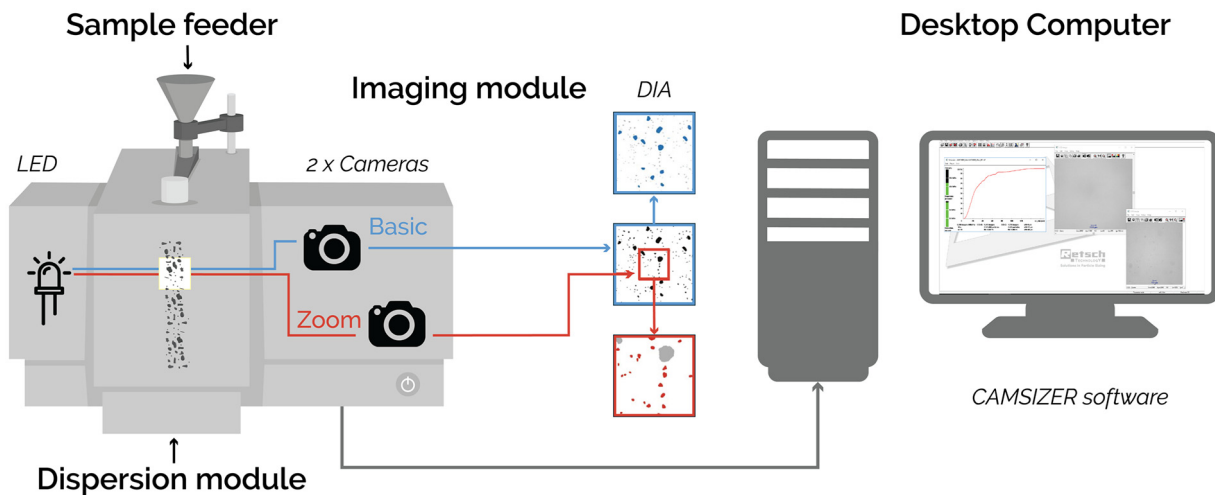


Fig. 1. Modular set up of CAMSIZER® X2 modified from Microtrac MRB (2020).

(10 µm to 8 mm), X-jet covers 0.8 µm – 5 mm and X-flow is suited to fine material (0.8 µm – 1 mm). The choice between X-jet and X-flow for fine material (0.8 µm – 1 mm) depends on the maximum grain size and amount of material available to be analysed. The X-flow uses only a very small amount (<10 mg) of material for analysis so is best suited to volume-limited fine-grained samples. The choice of dispersion method for coarse material (1–8 mm) depends on whether sample recovery is required, which is only possible for the X-fall.

For every analysis, the CX2 requires a 'task file' (Castro and Andronico, 2008) that informs the software of the analytical conditions to use and allows the user to customise the data acquisition. For example, particles with certain characteristics (e.g., related to size or shape parameters) can be excluded; this is useful for eliminating contaminating fibres which have extreme values of shape parameters such as compactness and convexity (Table 2). One important feature of the task file is whether a 'velocity adaption' is required. When using the X-fall module (free falling particles), a correction is needed to account for large particles falling faster than small particles under gravity, which causes them to be undercounted as they remain in the field of view of the camera for less time. In contrast, the X-jet dispersion mechanism requires the software to correct for small particles moving faster in the stream of compressed air relative to large particles. The user generates the velocity adaption within the CX2 software by producing a calibration curve of particle size versus particle

velocity. Best practise is to produce a new velocity adaption for samples where there is a broad GSD, and for samples that have not been analysed using the CX2 before (i.e., where there no pre-existing task file).

3.1.2. Principles of dynamic image analysis

The raw images captured by the basic and zoom cameras are converted to binary images (particle versus no particle). The size and shape of the particles in each image are measured by the CX2 software using an algorithm that combines the results from the basic and zoom cameras (Supplementary S1). Every particle imaged above a minimum size threshold is measured, with the minimum size determined by the limit of image resolution or the limit set in the task file. The software has the capacity to measure 100's of millions of particles at >300 images per second and can measure multiple size and shape parameters per particle (Table 2; Microtrac MRB, 2020). Three key size parameters are equivalent circle diameter (x_{area}), minimum chord diameter ($x_{c,min}$) and maximum Feret diameter ($x_{Fe,max}$; Table 2; Fig. 2). These parameters are not identical for irregular particles and therefore yield different information about the particle distribution. Importantly, computing all three size parameters allows CX2 outputs to be compared with different grain size measurement methods. For example, laser diffraction using Mie theory outputs equivalent sphere diameters (~ x_{area}) while cryptotephra data report the long axis ($x_{Fe,max}$) and the retaining

Table 2

Size and shape parameters used by the CAMSIZER® X2 software.

Notation or symbol	Name	Definition or formula	Alternative nomenclature
A_p	Area of particle		
A_{CH}	Area of bounding convex hull		
U	Perimeter		
r_1 and r_2	Particle radii	Minimum and maximum radii of a particle from the centre of the particle area	
x_{area}	Equivalent circle diameter	Diameter of the circle having the same projection area of the particle	
X_{Fe}	Feret diameter	The perpendicular distance between parallel tangents touching opposite sides of the profile	Length, caliper diameter
$x_{c,min}$	Chord diameter	Minimum width of the particle	Width, minimum rope
X_{Ma}	Martin diameter	Line bisecting the area of the particle	
SPHT	Sphericity	$\frac{4\pi A_p}{U^2}$	Form factor (Liu et al., 2015)
b/l	Aspect ratio	$x_{c,min}$	Width to length ratio, axial ratio (Liu et al., 2015)
CVX	Convexity	$x_{Fe,max}$	Solidity (Liu et al., 2015), roughness
CPT	Compactness	$\frac{A_p}{A_{CH}}$	Roundness (Liu et al., 2015)
Symm	Symmetry	$\sqrt{\frac{4A_p}{\pi}}$	
		$\frac{1}{2} \left[1 + \min(\frac{r_1}{r_2}) \right]$	

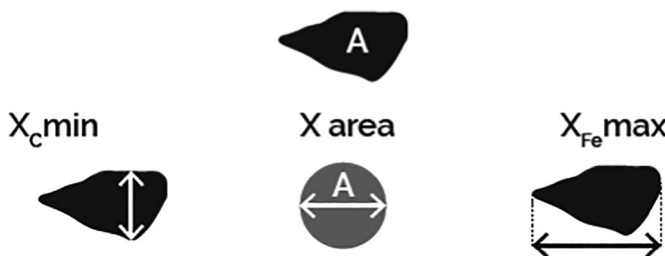


Fig. 2. Schematic of three key size parameters; $x_{c\min}$ the minimum chord diameter, x_{area} the equivalent circle diameter and $x_{\text{Fe}\max}$ the maximum Feret diameter.

sieve aperture should be greater than or equal to the minimum diameter of a particle ($x_{c\min}$; Freret-Lorgeril et al., 2019).

To obtain a GSD using the CX2, the results of the 2D image analysis are converted to 3D by calculating an apparent volume per particle. The conversion from area to volume depends on the size parameters chosen. Using x_{area} , the conversion to volume assumes spherical particles, whereas using $x_{\text{Fe}\max}$ and $x_{c\min}$ assumes ellipses where the long and short axes are represented by $x_{\text{Fe}\max}$ and $x_{c\min}$ respectively (Castro and Andronico, 2008). The data can be output as a GSD in terms of volume fraction or as a particle number distribution (PND; number of particles in each size fraction).

3.1.3. Post-processing and data analysis

The CX2 software has flexible data processing that allows adjustable binning of raw data (logarithmic or arithmetic). This means that there are no restrictions equivalent to those that arise from fixed sieve intervals. The software outputs the GSD as a probability density function and cumulative distribution function (PDF and CDF), and has customisable data visualisation options. The output of the CX2 software is a 'resource description framework' file (.rdf), that can be output as a Microsoft Excel compatible file (.xle) for user-specific data processing and analysis. Images can also be saved.

Another useful feature in the CX2 software is the 'particle wizard' tool, which crops the saved images to allow visualisation of individual particles. This can be helpful for ensuring the task file has been designed correctly. For example, particles with specific shape and size characteristics can be displayed to confirm that contaminants (such as fibres) are identified and eliminated from the GSD. The particle wizard is also useful for qualitatively characterising particle shapes in different size fractions.

To facilitate flexible and reproducible data processing and visualisation, we analyse sample GSDs in Microsoft Excel and R. We output each GSD from the CX2 in two grain size bin configurations, one equivalent to a half- φ scale for compatibility with sieve data, and one on the linear scale with a bin width of 5 μm . For all GSDs we compute the Folk and Ward, 1957 graphical parameters of mean (μ_{FW}), standard deviation or sorting (σ_{FW}), skewness (Sk) and Kurtosis (K). We also fit log-normal and Weibull distributions directly to the GSDs using the 'fitdistrplus' package in R (Delignette-Muller and Dutang, 2015). Mixture models of log-normal and Weibull distributions were fit to multimodal GSDs using the 'mixfit' function from the 'mixR' R package (Yu, 2018). The probability density functions, and distribution fitting methods are reported in Appendix B.

3.2. Test samples and method comparison

3.2.1. Sample preparation and data collection

To test the capabilities and performance of the CX2, we conducted a series of preliminary analyses with fixed shape samples including glass spheres (ballotini), sub-spherical, disc- and rod-shaped particles. We also analysed natural samples that had been characterised using other techniques. Prior to analysis, some sample preparation was required.

To gauge the approximate size, the ballotini were dry sieved into 6 sieve fractions using disposable nylon sieve meshes to ensure no contamination: >500 μm , 355–500 μm , 100–250 μm , 65–110 μm , 50–65 μm and 20–50 μm . The natural samples include Mazama tephra (~7.7 ka eruption of Crater Lake, OR, USA) sampled at different distances from source (Buckland et al., 2020), hydromagmatic fallout samples from the Hverfjall Fires (~2.5 ka eruptive episode of Krafla Volcanic System, Iceland) sampled by Liu et al. (2017), distal Campanian Ignimbrite tephra (~39 ka eruption from Phlegraean Fields, Italy) sampled by Engwell et al. (2014), and tephra from the 1980 eruption of Mount St. Helens (MSH), Washington, USA sampled via multiple sources (Meredith, 2019). Some of the MSH samples are assumed to be equivalent to samples analysed by other authors (Sarna-Wojcicki et al., 1981; Durant et al., 2009) based on comparable sampling locations (Supplementary S2). The tephra was dried to eliminate particle cohesion (Castro and Andronico, 2008) and dry sieved into half- φ intervals from 8 mm – 125 μm (–3 to 3 φ) where necessary. Further information on the natural samples can be found in the supplementary information.

3.2.2. Choice of size parameters

To explore the reliability of the different size parameters calculated by the CX2, we measured the ballotini sieve fractions using x_{area} , $x_{\text{Fe}\max}$ and $x_{c\min}$ (Fig. 2). As expected, the choice of size parameter for the ballotini did not significantly alter the GSD in any sieve fraction (Fig. 3a) because x_{area} , $x_{\text{Fe}\max}$ and $x_{c\min}$ are equal for spherical particles (equivalent to circular in 2D images; Fig. 3c). The near vertical cumulative distributions reflect the manufacturing of the ballotini to achieve narrow GSDs and the efficacy of pre-analysis sieving. There is a slight fine tail in two of the analyses (Fig. 3a) that could indicate imperfect sieving where the finer material had not fully segregated into the correct sieve fraction. The largest variability in size parameter is observed in the $x_{\text{Fe}\max}$ data. This is attributed to the presence of slightly elongated spheres which we observed with optical microscope images (Fig. 3b). Similarly, the coarsest sieve fraction contained some irregular particles (Fig. 3c), which are likely a manufacturing fault.

We repeated this analysis on non-spherical fixed shape particles and sieved natural samples to further explore the sensitivity of GSDs to size parameter (Figs. 4 & 5; Supplementary S3). Non-spherical particles, including volcanic tephra, have GSDs that vary according to the size parameter as reflected in the grain size statistics. For example, the median $x_{c\min}$ of the rod-shaped particles is 1800 μm compared to 6400 μm when size is measured as $x_{\text{Fe}\max}$. Similarly, the median size of the disc-shaped particles ranges from 3200 μm ($x_{c\min}$) to 3700 μm ($x_{\text{Fe}\max}$). The sensitivity of GSDs to size parameter is also observed within the individual sieve fractions of tephra. Interestingly, GSDs quantified by $x_{c\min}$ are closest to the expected sieve range according to sieve diameter d . Extending the sieve range so that the maximum grain size is equal to the hypotenuse of the sieve aperture shows better agreement with the x_{area} GSD (Fig. 4b), consistent with comparisons between optical image analysis (Morphologi GS3) and sieving (Freret-Lorgeril et al., 2019). In contrast, the coarse tail on the $x_{\text{Fe}\max}$ GSD extends well beyond both sieve ranges, indicating that elongated particles can pass through the sieves on their intermediate or short axes. The x_{area} and $x_{\text{Fe}\max}$ distributions within a size fraction also vary between samples (Fig. 4). For example, the median $x_{\text{Fe}\max}$ of the Campanian Ignimbrite 2 φ sieve fraction is 512 μm , compared to a median $x_{\text{Fe}\max}$ of 427 μm for the same sieve fraction of Mazama tephra. Similar to the ballotini analyses (Fig. 3), the observation that all GSDs of the natural samples have fine tails below the sieve range signifies that fine material is often retained in coarse sieves due to imperfect segregation as a result of the aggregation of fines or the adhesion of fine material to larger particles.

3.2.3. Shape parameters and distributions

The CX2 measures multiple shape parameters. Three shape parameters measured on the fixed shape particles and natural samples were

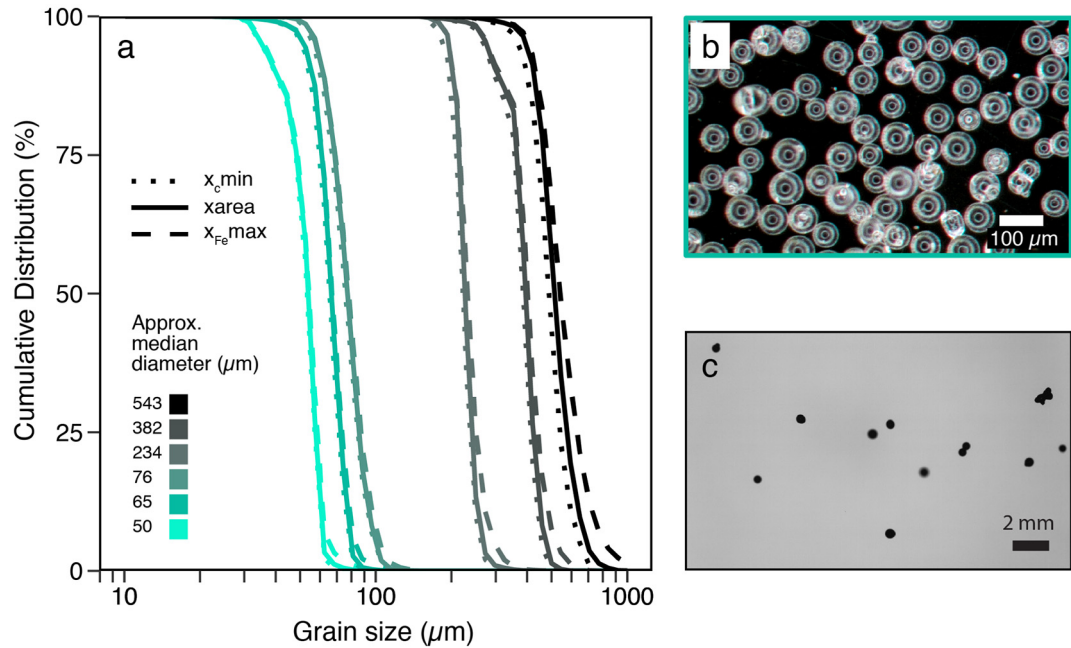


Fig. 3. Comparing the size parameters for six ballotini size fractions. a) Cumulative grain size distributions showing that the three size parameters (differentiated by the line pattern) plot close to on top of each other for each size fraction (differentiated by the line colour). b) Optical microscope image of the 65–110 μm sieve fraction. c) CX2 image from the DIA of the $>500 \mu\text{m}$ sieve fraction.

sphericity (SPHT; $\frac{4\pi A_p}{U^2}$), symmetry (Symm; $\frac{1}{2} \left[1 + \min \left(\frac{r_1}{r_2} \right) \right]$) and aspect ratio (b/l; Table 2). For perfectly spherical particles these parameters should equal 1 for all grain sizes. However, small imperfections and deviations from perfect spheres will reduce these shape parameters to <1 and each has a different sensitivity. For example, the interpretation that the $x_{\text{Fe}}\text{max}$ results (Fig. 3) for the coarser ballotini contained a larger proportion of non-spherical particles is supported by the lower mean values of both symmetry (0.95) and aspect ratio (0.87) compared to the finer ballotini (Symm = 0.97, b/l = 0.96). In contrast, there is no significant change in the range of SPHT, a parameter that is sensitive to particle perimeter (roughness), with grain size for the ballotini, suggesting that the deviations from perfect spheres arise primarily from elongation and surface protrusions rather than surface roughness (Fig. 3c; Supplementary S3).

Shape data are also susceptible to differences in image resolution, which becomes a problem when samples span a wide size range (e.g., Saxby et al., 2020). For example, the large number of pixels per particle for coarse particles could increase the particle perimeter measurement relative to the particle area, which would artificially lower the SPHT. Nevertheless, our data on ballotini show little relation between particle size and the SPHT (Supplementary S3) and we attribute the changes in Symm and b/l with grain size to imperfections in the ballotini rather than differences in image resolution.

Shape distributions measured for the non-spherical test particles and the natural tephra samples show that the CX2 can be used to differentiate samples according to particle shape (Figs. 5 & 6). For example, analysis of rod-shaped glass beads generated an average aspect ratio (b/l) of 0.32, which is close to the value expected from the manufacturer size specifications (~0.3). Due to the varied orientation of the particles relative to the imaging module, however, the CX2 method can underestimate the size and shape of some particles. This is particularly evident in the analyses of disc-shaped particles where the shortest dimension is rarely perpendicular to the imaging module; this means that x_{cmin} and thus the aspect ratio, is overestimated (Fig. 5c; CX2 b/l ~ 0.7 versus real b/l ~ 0.3). However, the large number of particles measured by the CX2 means that the shape parameters and distributions still reflect the non-sphericity of particles which is evident in the shape distributions

for natural samples (Fig. 6; $n \sim 10^8$ particles per tephra analysis; see supplementary data).

Compared to the ballotini, the sieved Campanian Ignimbrite, Hverfjall and Mazama tephras show a wide range of SPHT values as a result of the irregular particle morphology (Fig. 6a). The Mazama distribution shows the highest SPHT values as it contains a high proportion of free crystals with smooth surface textures compared to the basaltic Hverfjall and micro-pumice rich Campanian Ignimbrite tephras (Fig. 6a). Interestingly, bimodal and unimodal MSH samples display different SPHT distributions (Fig. 6b); here bimodal samples have been interpreted to record particles produced by different phases of the eruption (Eychenne et al., 2015). The aspect ratio (b/l), which reflects the elongation of particles, is lowest for the Campanian Ignimbrite tephra but shows no real difference between the Hverfjall and Mazama tephras (Fig. 6c).

3.2.4. Comparison of CAMSIZER X2 results with other methods

The GSD of the natural samples has been previously characterised using a combination of sieving and laser diffraction (Mount St. Helens, Durant et al., 2009; Campanian Ignimbrite, Engwell et al., 2014; Hverfjall Fires, Liu et al., 2017; Mazama, Buckland et al., 2020). Here we compare the GSDs of fine-grained tephras measured using laser diffraction with GSDs measured using DIA with X-jet and X-flow dispersion mechanisms (Fig. 7). We expect the xarea CX2 GSDs to be the most comparable to GSDs from laser diffraction if Mie scattering theory (Appendix A) is used (Fig. 7a-b). The Campanian Ignimbrite GSD measured by laser diffraction used the Fraunhofer approximation (Appendix A) and appears to be best matched by $x_{\text{Fe}}\text{max}$ in the CX2 GSD (Fig. 7c). The laser diffraction GSDs consistently have a broader fine-grained tail than the CX2 results (Fig. 7). For example, laser diffraction suggests that 10% of the volume of the MSH tephra is $<4 \mu\text{m}$ whereas the X-jet GSD quantified as xarea suggests that 10% of the sample is $<8 \mu\text{m}$ (Fig. 7b). The X-jet and X-flow GSDs also differ slightly at the coarse end of the distribution with the X-flow distribution showing that $<5\%$ of the Mazama tephra is coarser than $100 \mu\text{m}$ while the laser diffraction and X-jet distributions show that $>10\%$ of the sample is coarser than $100 \mu\text{m}$ (Fig. 7a).

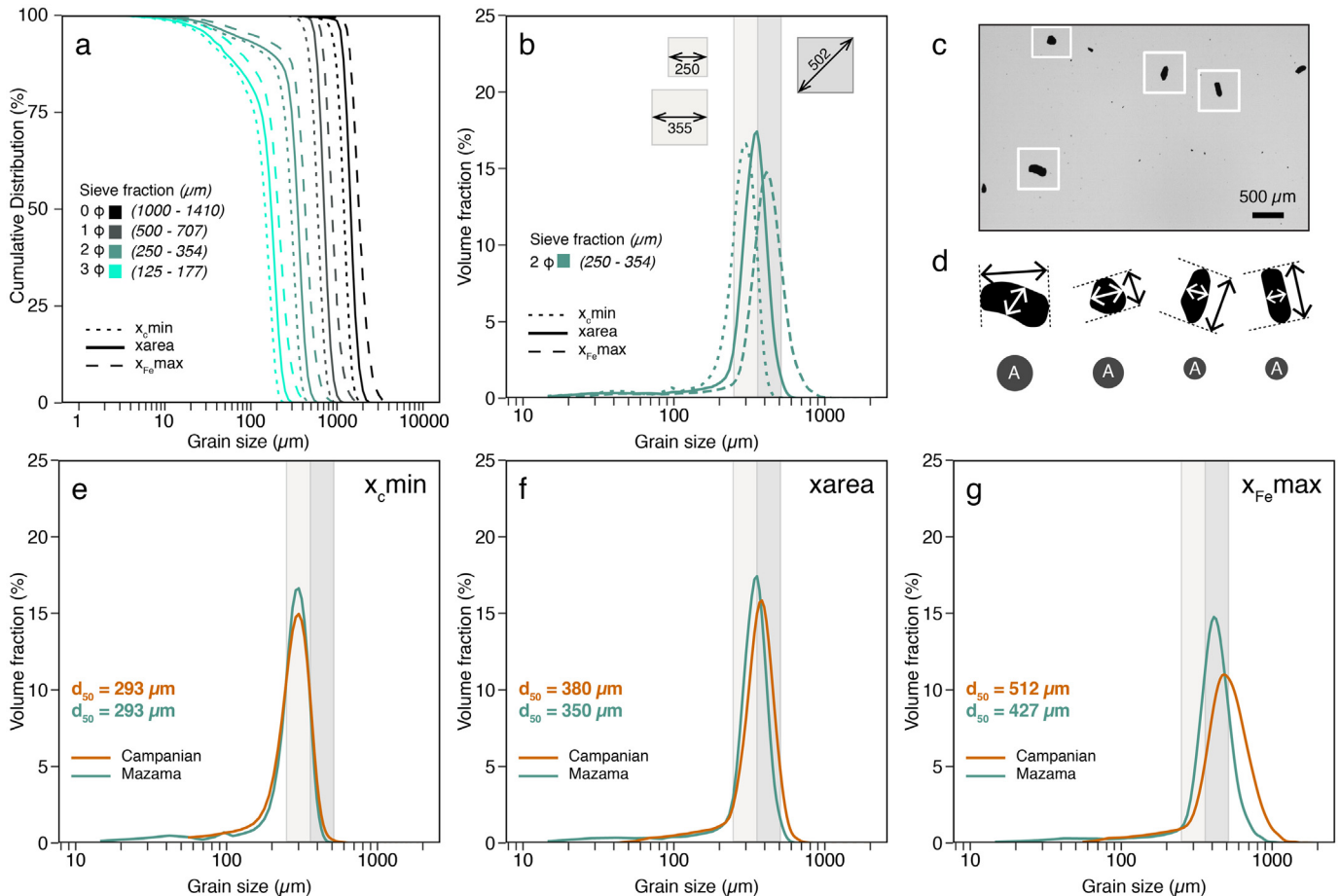


Fig. 4. Comparing different size parameters for natural sieved tephras. a) Cumulative GSDs for Mazama tephra showing the three size parameters (differentiated by the line pattern) for each half- ϕ sieve fraction (differentiated by the line colour). b) GSDs of the 2 ϕ (250–354 μm) sieve fraction for each size parameter. The light grey box indicates the size range expected from sieving according to sieve diameter; the dark grey box extends this range to the length of the sieve aperture hypotenuse. c) CX2 image from the DIA (using X-Jet) of the 2 ϕ sieve fraction of Mazama tephra. d) Binary images of irregular Mazama tephra particles from c) with $x_{\text{Fe max}}$, $x_{\text{c min}}$ and x_{area} indicated. e-g) Comparing GSDs within a sieve fraction according to the size parameter for the Mazama and Campanian Ignimbrite tephras.

In Fig. 7, the differences between the CX2 and laser diffraction at the $<10 \mu\text{m}$ end of the scale are due to the different minimum particle sizes measured by the instruments. Laser diffraction detects particles $>0.01 \mu\text{m}$, whereas the lower size limit of the CX2 is 0.8 μm . For very fine-grained material ($<10 \mu\text{m}$) there are also some limitations of laser

diffraction. For example, fine material can cause multiple scatterings of the laser beam, and some authors have attributed an overestimation of fine particles to the presence of non-spherical grains (Vriend and Prins, 2005; Jonkers et al., 2009). The differences in the GSDs $>100 \mu\text{m}$ are likely the result of the amount of material analysed. The X-jet

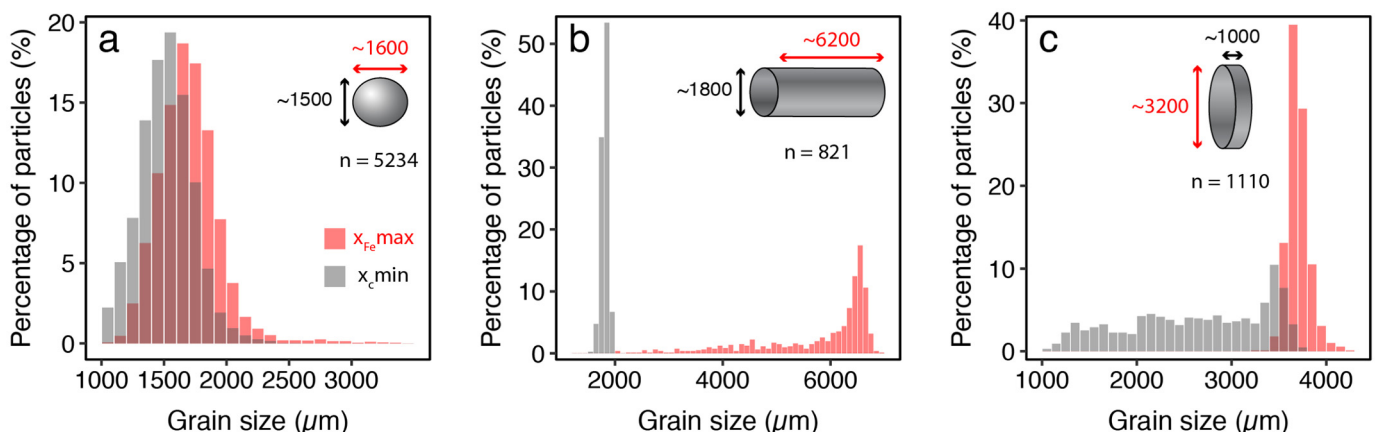


Fig. 5. The impact of particle shape on size and shape parameters. Particle number distributions according to $x_{\text{Fe max}}$ and $x_{\text{c min}}$ for a) sub-spherical particles, b) cylindrical particles and c) disc shaped particles. The diagrams show the 3D shapes and approximate dimensions with n equal to the number of particles analysed.

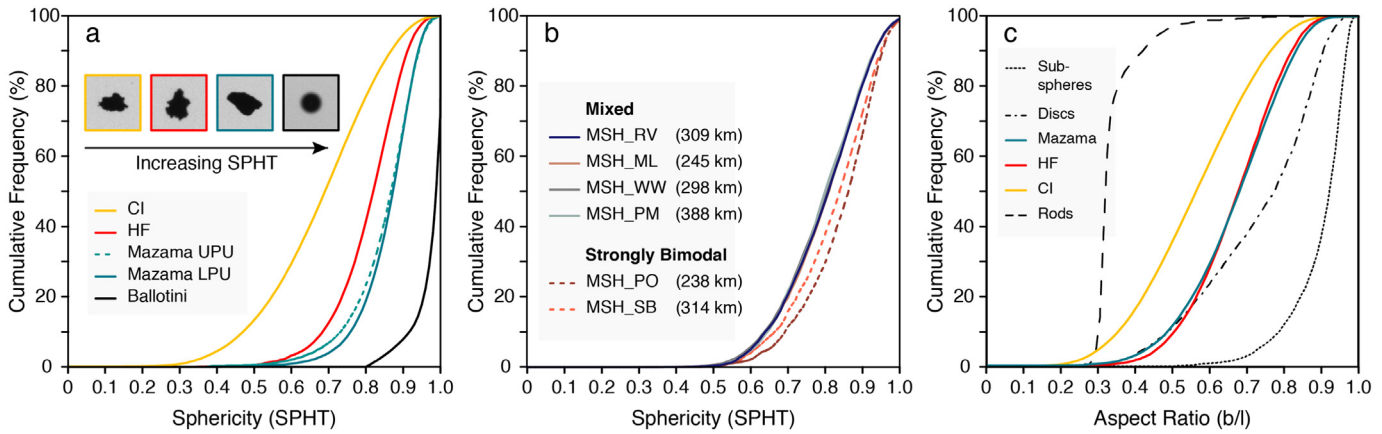


Fig. 6. Cumulative shape distributions for ballotini and natural samples: Campanian Ignimbrite (CI), Hverfjall Fires (HF), Mazama Upper and Lower Pumice Units (UPU, LPU) and Mount St. Helens (MSH). a) Comparing SPHT for individual sieve fractions of ballotini and natural tephra samples. The 2.5φ sieve fraction ($180\text{--}250\mu\text{m}$) is shown for the natural samples, and the ballotini data is for the sieve fraction with $234\mu\text{m}$ median diameter. b) SPHT distributions for distal MSH samples. c) Comparing b/l distributions for the 2.5φ sieve fraction of natural tephra samples and fixed shape particles.

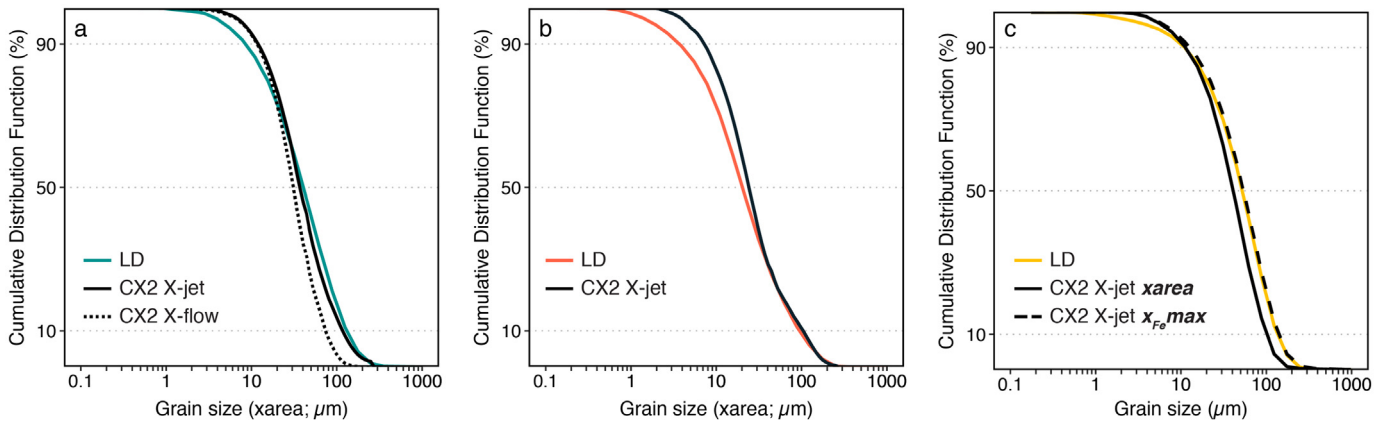


Fig. 7. Comparing GSDs from laser diffraction (LD) with CX2 GSDs for fine-grained distal tephras. a) GSDs for distal Mazama sample from site 73. b) GSDs for distal MSH sample. Laser diffraction analysis carried out on sample DAVIS11 by [Durant et al. \(2009\)](#), corresponding sample MSH_RV analysed using CX2 for this study (see Supplementary S1). c) GSDs for ultra-distal Campanian Ignimbrite tephra. Laser diffraction analysis from [Engwell et al. \(2014\)](#) compared to X-jet GSDs according to size parameter.

method analyses the largest volume of material; this ensures representative sampling of coarse particles, unlike the wet dispersion methods which use a small amount of material per analysis and are thus more likely to underrepresent coarse particles. Importantly, small differences in the number of large particles can translate to considerable variability in volume-based GSDs because of the large contribution of coarse particles to the total sample volume.

For the coarser Mazama tephra, we compare GSDs measured using a combination of sieving and CX2 (X-jet) with GSDs produced using the CX2 alone, where the X-fall ($>125\mu\text{m}$) and X-jet ($<125\mu\text{m}$) analyses are combined (Fig. 8). The sieve and CX2 data were combined using the overlap between the methods at $125\text{--}250\mu\text{m}$ by assuming a constant particle density and therefore converting the volumetric size distribution (CX2) to a mass distribution (e.g., [Eychenne et al., 2012](#)). The X-fall and X-jet data were combined by weighting the coarse and fine distributions according to the mass percentage that was greater than and less than $125\mu\text{m}$. For the sake of comparison, all data were processed in half- φ intervals to match the limits of data manipulation imposed by sieving.

The difference between the GSDs in Fig. 8 results from the distinction between coarse GSDs that are quantified as weight percent (mass%); sieving & CX2) versus volume percent (vol%; CX2). The GSDs obtained from sieving have a strong mode at $2\text{--}1.5\varphi$ ($250\text{--}354\mu\text{m}$), which corresponds to the sieve fraction that contains a large proportion of

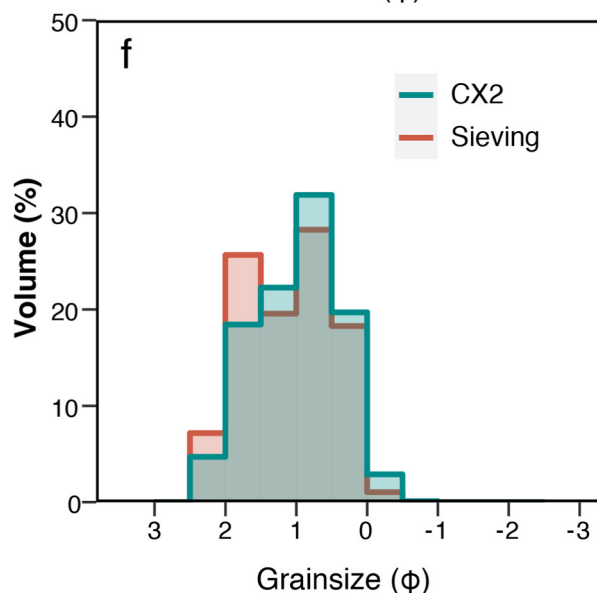
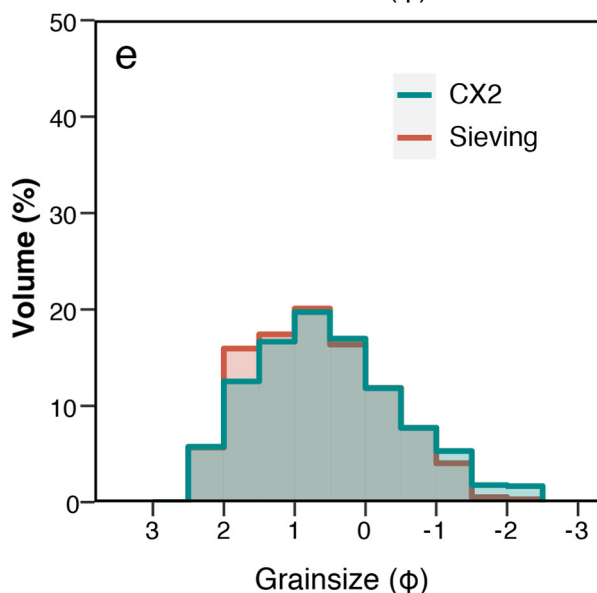
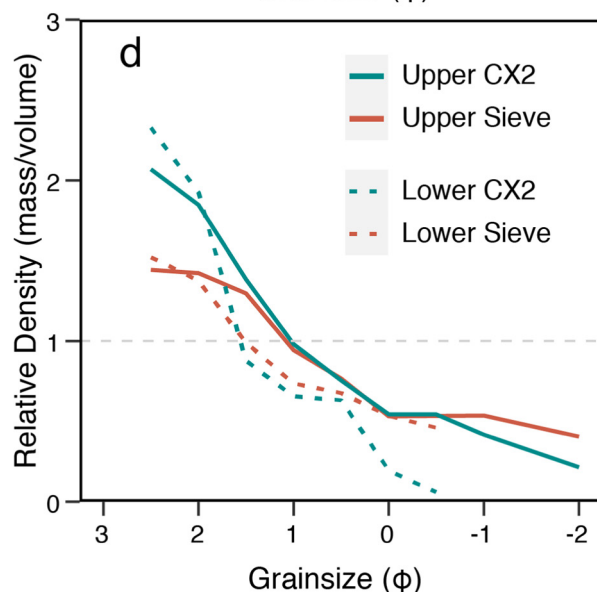
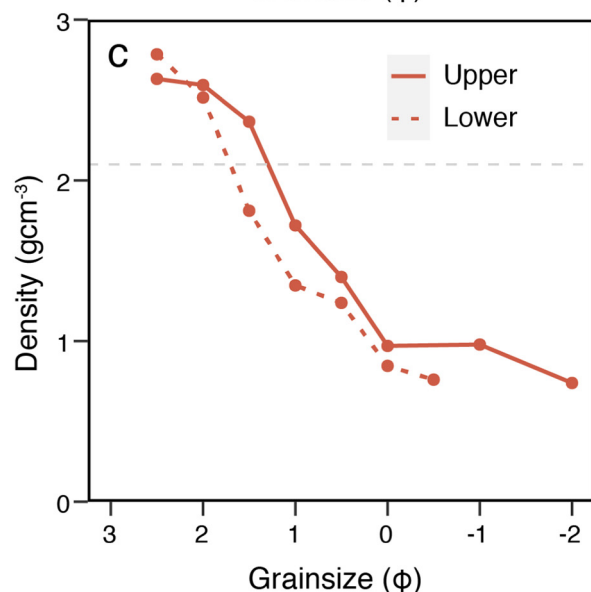
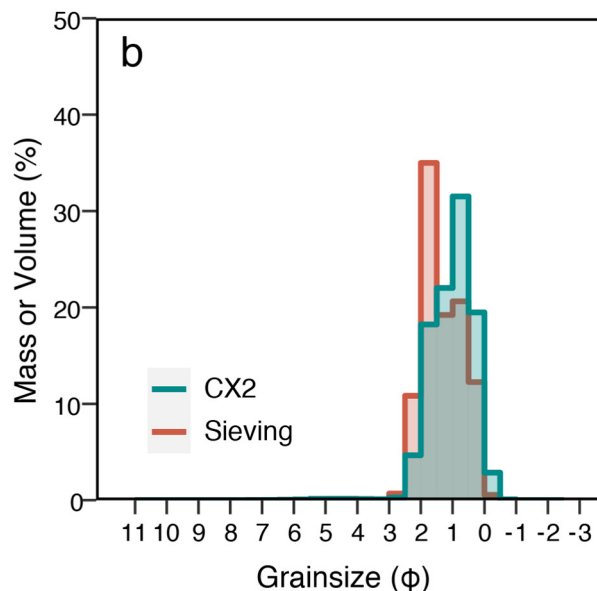
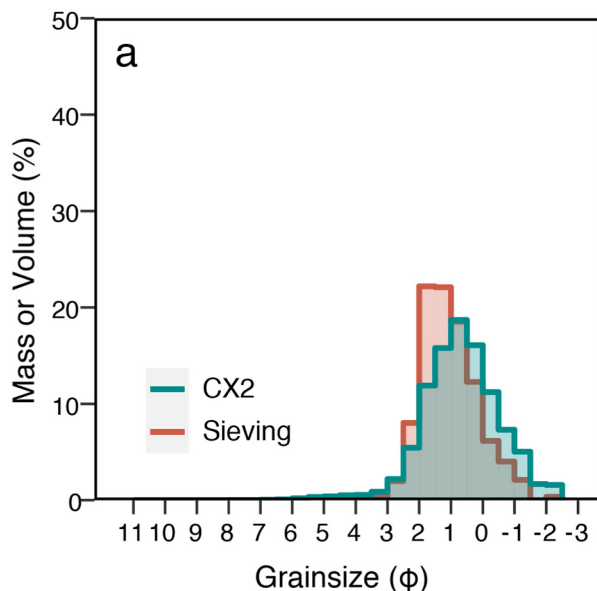
dense phenocrysts (magnetite and pyroxene); this mode remains constant throughout the Mazama tephra section (upper and lower pumice fallout units). The modes in the CX2-only distributions (Figs. 8a-b) do not align with the GSDs from sieving because they are represented in terms of the vol% (rather than mass%) in each size class. This means that although the X-fall and X-jet analyses are combined by the relative mass% $>$ and $< 125\mu\text{m}$, dense individual size fractions (crystal concentrations) do not manifest as the mode of the GSDs.

4. Results

The method development and testing reviewed in section 3 show that the CX2 provides an appropriate analytical protocol for characterising the grain size and morphology of volcanic tephra up to 8 mm ($\geq -3\varphi$). Here we explore the unique capabilities of DIA for determining GSDs of samples with non-uniform density distributions and then examine the sensitivity of grain size statistics to the choice of size parameter and method of grain size measurement.

4.1. Non-uniform density distributions

The CX2 and sieve analyses of the coarse Mazama tephra differ because of the non-uniform density of the pyroclasts across the GSD (Fig. 8). In contrast, parallel sieve and CX2 analyses of natural tephras



with less significant changes in clast density show similar GSDs when quantified by either mass or volume (Supplementary S3). This contrast suggests we can use simultaneous measurements of GSDs by mass and volume to invert for density distributions.

To obtain independent measurements of density, we used a water pycnometer (e.g., Eychenne and Le Pennec, 2012; Liu et al., 2017) to analyse the $-2 - 2.5 \varphi$ sieved size fractions of Mazama samples from the upper and lower pumice units (Fig. 8c). These data show the expected increase in particle density with decreasing size (Bonadonna and Phillips, 2003; Eychenne and Le Pennec, 2012) but also highlight the high density ($\rho \sim 2.6 \text{ g cm}^{-3}$) of the 2 and 2.5φ sieve fractions where pyroxene and magnetite crystals are concentrated, a density that greatly exceeds that of the matrix glass ($\sim 2.1 \text{ g cm}^{-3}$). We used the sieved mass and measured density of each size class to calculate a volume-based GSD to compare with the CX2 GSD (Fig. 8e-f). This comparison shows that relative to the sieve data, the CX2 underestimates the volume in the sieve fractions ($1.5 - 2.5 \varphi$) that contain the dense crystals and overestimates the volume of the coarse pumice clasts. For example, sieve data show that 16% of Mazama upper pumice sample is in the 2φ sieve fraction compared to 12% according to the CX2 GSD (Fig. 8e). This difference is reflected in the relative density calculated by dividing the mass % by the volume % in each class (Fig. 8d). Importantly, whilst the resulting absolute values of relative density diverge for sieve and CX2 data, the relative density profiles derived from the CX2 data clearly show the presence of dense crystal-rich grain size fractions ($3 - 1.5 \varphi$) compared to the coarse low-density pumice clasts ($< 1.5 \varphi$). These data illustrate the important information about the particle population that can be determined from a direct comparison of mass and volume.

4.2. Grain size distribution statistics

Grain size statistics provide a way to quantitatively compare GSDs that arise from different measurement methods. For example, the Folk and Ward (1957) mean grain size (μ_{FW}) calculated for the Mazama upper pumice is 1.07φ ($476 \mu\text{m}$) for sieve data compared to 0.38φ ($768 \mu\text{m}$) for the CX2 GSD (Table 3). Similarly, for fine-grained Mazama samples (Fig. 7), μ_{FW} varies from $4.73 - 5.38 \varphi$ ($38 - 24 \mu\text{m}$) depending on the size parameter ($x_{c,\min}$ or x_{area}) and method of grain size analysis used (laser diffraction or CX2; Table 3). The FW sorting (σ_{FW} ; measure of spread) and skewness (Sk ; measure of symmetry) also depend on the method used (Table 2). For example, the Sk of the lower pumice is -0.20 when measured by sieving but $+0.15$ when measured with the CX2. This difference affects the qualitative classification from finely skewed (sieving) to coarsely skewed (CX2; Table B1). Another important parameter is the proportion of fine ($< 125 \mu\text{m}$) and very fine ($< 15 \mu\text{m}$) ash. Here the proportion of very fine ash ($< 15 \mu\text{m}$) in sample MZ73 ranges from 16% (x_{area} ; X-jet) to 26% ($x_{c,\min}$; X-flow) of the total volume.

The statistics and interpretation of multimodal GSDs are similarly sensitive to the method used to characterise the distribution (Fig. 9; Table 4). The distal MSH ash has previously been shown to contain at least two grain size sub-populations (Durant et al., 2009; Eychenne et al., 2015). Deconvolution of GSDs into subpopulations, however, is sensitive to differences in both the starting GSD and the distribution chosen (log-normal or Weibull; Appendix B). We illustrate this difference using PDFs deconvolved for the laser diffraction GSD compared to the CX2 GSD (Figs. 9c&f). When the number of log-normal subpopulations is fixed at 2, the laser diffraction GSD (Fig. 9a) is resolved into distributions with means of 9.23φ ($2 \mu\text{m}$) and 5.47φ ($26 \mu\text{m}$). The

same fitting algorithm applied to the CX2 GSD resolves two sub-populations with means of ~ 5.6 and 3.0φ (21 and $125 \mu\text{m}$) respectively (Fig. 9b; Table 4). This comparison shows that two samples from the same deposit, taken from the same location, can have GSDs that can be interpreted differently simply because of measurement method.

It is well known that grain size statistics are also sensitive to bin size. To explore this sensitivity, we processed the data in multiple bin configurations (Table 4). We find that fitting of unimodal and bimodal distributions is not strongly affected by the type of binning used, particularly when working with fine-grained material (Fig. 9d-f). However, coarse bins are still problematic for particles $> 500 \mu\text{m}$ when using the φ -scale, which translates into a wide range on the linear scale and poor resolution of the distribution within the sieve intervals (Hails et al., 1973). Similarly, coarse linear binning ($> 5 \mu\text{m}$) can obscure the GSD in the fine grain sizes and places too much emphasis on the coarse particles (Blott and Pye, 2001).

5. Discussion

The CX2 is a valuable tool for simultaneously analysing the size and shape of non-spherical particles, such as tephra, thanks to the dynamic image analysis (DIA) principle. Here we discuss some of the benefits of DIA relative to more widely used methods of grain size analysis (see section 2; Table 1; Appendix A). We also consider the limitations of grain size analysis methods, in particular, for studying ultra-fine ($< 10 \mu\text{m}$) particles. Finally, we discuss the implications of different grain size methods for using and interpreting grain size data for the purposes of studying explosive volcanism.

5.1. Appraisal of dynamic image analysis for measuring non-spherical particles

DIA facilitates rapid and simultaneous quantification of the size and shape of tephra whilst other particle analysis techniques compromise on either particle shape information or analysis time. For example, laser diffraction contains no shape information but is fast (~minutes), whereas SEM image analysis provides excellent particle shape data but can require pre-analysis sample preparation (sieving) and substantial image processing (~hours-days). DIA has the added benefit of measuring multiple size descriptors (Figs. 2–5). Comparing GSDs quantified by different size parameters supplements shape parameterisation as the disparities between the GSDs can be used to infer the presence of extreme particle shapes (Figs. 4–5).

Quantifying different size parameters can also explain some of the grain size anomalies described in the literature. For example, the large grains reported in cryptotephra studies (Stevenson et al., 2015; Saxby et al., 2019) are quantified according to their $x_{Fe,\max}$ size. Our data show that within individual sieve classes particles can have $x_{Fe,\max}$ values that extend well beyond the range predicted by the sieve aperture (Fig. 4). In other words, sieve data can mask extreme particle sizes if the maximum particle dimension is assumed equal to the passing sieve aperture. Furthermore, we have confirmed that the size parameter measured by sieving depends on particle shape. For example, elongated particles are most commonly sorted according to their minimum dimension ($x_{c,\min}$), however, platy particles such as found in the Campanian Ignimbrite tephra, are sorted by their intermediate dimension. This has implications for converting from sieve aperture to particle volume as it will lead to the overestimation of particle volume for most non-spherical particles.

Fig. 8. Comparing GSDs of Mazama tephra measured by sieving & CX2, with CX2 alone. All samples are from a fallout section located at site 46–120 km from source (see supplementary information S1). a) Sample from the upper pumice unit, b) sample from the lower pumice unit. c) Measured densities (g cm^{-3}) of individual sieve fractions for the upper and lower unit with the dashed line indicating the density of Mazama glass $\sim 2.1 \text{ g cm}^{-3}$. d) The relative density of half- φ sieve fractions calculated using the sieve data (red) and the CX2 & sieve data (blue). e) and f) Comparing the volume distributions measured using the CX2 with calculated volume distributions from sieve data for the upper (e) and lower (f) units between $2.5 - 2.5 \varphi$.

Table 3Grain size statistics calculated for different methods of grain size analysis.^a

Sample	Method	Binning	$\mu_{FW} (\phi)$	$\sigma_{FW} (\phi)$	Sk_{FW}	<125 μm (%)	<15 μm (%)
MZ46 Upper Pumice (Fig. 8a)	Sieving & CX2	$1/2 \phi$	1.07	0.92	-0.15 (coarse skewed)	2.4	0.2
	CX2 ($x_c\min$)	$1/2 \phi$	0.66	1.15	-0.04 (symmetrical)	2.4	0.2
MZ46 Lower Pumice (Fig. 8b)	Sieving & CX2	$1/2 \phi$	1.32	0.67	-0.20 (coarse skewed)	0.82	0.01
	CX2 ($x_c\min$)	$1/2 \phi$	1.00	0.65	0.13 (fine skewed)	0.84	0.01
MZ73	CX2	$1/4 \phi$	5.11	1.24	-0.01 (symmetrical)	95	23
	X-jet ($x_c\min$)	$1/4 \phi$	4.74	1.27	-0.01 (symmetrical)	91	16
	X-jet (x_{area})	$1/4 \phi$	5.38	1.01	0.06 (symmetrical)	99	26
	CX2	$1/4 \phi$	5.03	1.04	0.05 (symmetrical)	99	17
	X-flow ($x_c\min$)	$1/4 \phi$	4.73	1.53	0.14 (fine skewed)	89	20
	X-flow (x_{area})	$1/2 \phi$					
	LD	$1/2 \phi$					
	(x_{area})						

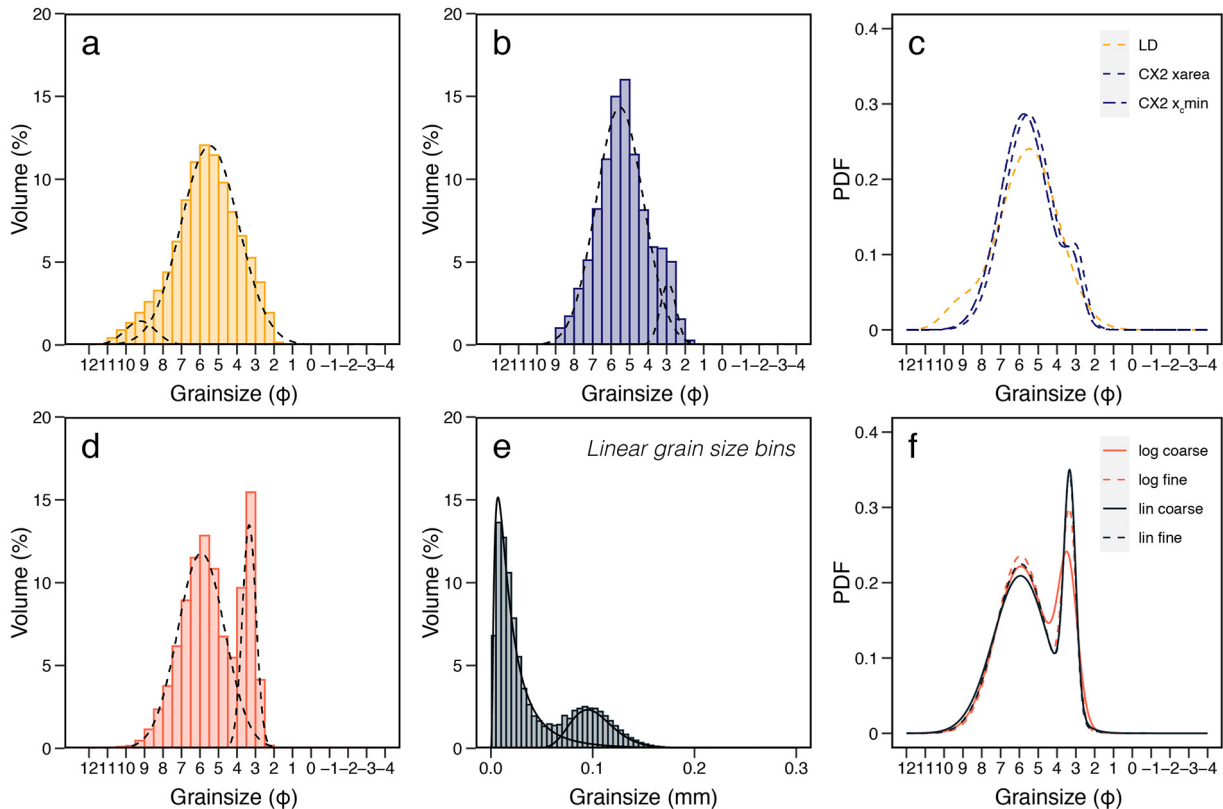
^a FW = Folk and Ward (1957) graphical method of calculating GSD statistics.

Fig. 9. Bimodal log-normal distributions fit to MSH GSDs. a) GSD of DAVIS11 measured with laser diffraction (Durant et al., 2009) fit with two log-normal subpopulations. b) GSD of MSH_RV measured by X-jet (x_{area}) fit with two log-normal subpopulations. c) Comparison between bimodal distributions according to method and CX2 size parameter. d) GSD of MSH_SB sample in half- ϕ bins with two log-normal subpopulations. e) GSD of MSH_SB sample binned on the linear scale (5 μm) fitted with two log-normal subpopulations. f) Comparison between distributions fit on the ϕ and linear scales, as well as coarse (full ϕ ; 10 μm) and fine bins (half ϕ ; 5 μm).

Collection of multiple size parameters allows comparison of DIA GSDs with other widely used grain size measurement methods. The $x_c\min$ parameter closely matches the expected sieve range (Fig. 4), meaning that there is limited data loss and manipulation required to combine coarse and fine-grained measurement methods. Laser diffraction (LD) estimates x_{area} when using Mie theory and x_{femax} when using the Fraunhofer approximation (Fig. 7). Aside from differences in

the finest grain sizes (<10 μm), CX2 and LD GSDs are comparable, which is advantageous for comparisons with established grain size datasets (e.g., Durant et al., 2009; Engwell et al., 2014; Liu et al., 2017).

An additional benefit of DIA is that it quantifies GSDs in terms of volume percent, such that coarse (>125 μm) GSDs can be compared directly with other volume-based methods of grain size analysis (laser diffraction, image analysis). This means there is no need to convert

Table 4

Main parameters of bi-modal MSH samples calculated using different methods of grain size analysis and different bin configurations. $\mu_{\phi 1}, \mu_{\phi 2}$ = log-mean, $\sigma_{\phi 1}, \sigma_{\phi 2}$ = log-standard deviation, p_1, p_2 = proportion of the total GSD of the fine- and coarse-grained sub-populations respectively.

Sample	Method	Binning	$\mu_{\phi 1}$	$\mu_{\phi 2}$	$\sigma_{\phi 1}$	$\sigma_{\phi 2}$	p_1	p_2
DAVIS11 ^a (Fig. 9a&c)	LD	$1/2 \varphi$	9.23	5.47	0.83	1.56	0.06	0.94
	(xarea)							
MSH_RV (Fig. 9b-c)	CX2	$1/2 \varphi$	5.53	2.92	1.28	0.43	0.92	0.08
	(xarea)							
MSH_SB (Fig. 9d-f)	CX2	$1/2 \varphi$	5.76	3.13	1.28	0.46	0.92	0.08
	(x,min)							
MSH_SB (Fig. 9d-f)	CX2	1 φ	5.92	3.42	1.35	0.50	0.75	0.25
		$1/4 \varphi$	5.93	3.34	1.27	0.37	0.75	0.25
		$1/4 \varphi$	5.93	3.34	1.25	0.32	0.74	0.26
		1 μm	5.94	3.36	1.25	0.32	0.75	0.25
		5 μm	5.92	3.33	1.35	0.31	0.76	0.24
		10 μm	5.94	3.32	1.45	0.31	0.76	0.24

^a DAVIS 11 sample was sampled very close to MSH_SB (Sarna-Wojcicki et al., 1981; Durant et al., 2009; Meredith, 2019).

between volume and mass which requires an assumption of particle density. The effect of variable particle density on GSDs is illustrated in Fig. 8, which shows that mass-based GSDs can be influenced by dense grain size fractions that arise from crystal concentrations. Fig. 8d also clearly highlights an abrupt increase in particle density that can be related to crystal concentration in the 2–3 φ size range. Importantly, disparities between the volumetric GSDs calculated from direct mass and density measurements and those measured using the CX2 (Fig. 8e-f) can be explained by the propagation of uncertainty in the density measurements (+/− 10%) as well as a limitation of the CX2 velocity adaptation when a wide range of particle densities exist in a narrow size range (see Supplementary S1). Whilst the relative density distributions calculated cannot be used quantitatively (Fig. 8d), this approach provides a fast way to qualitatively investigate changes in particle density and can be used to identify size classes that require direct density measurements, which are more accurate but time consuming.

Although DIA has clear advantages for characterising tephra it also has limitations. Firstly, the minimum grain size measured by the CX2 is 0.8 μm , which is coarser than laser diffraction techniques (e.g., the Mastersizer 3000 minimum size is 0.01 μm). Sub-micron and nano scale particles are important for understanding satellite retrievals of volcanic ash in the atmosphere (e.g., Prata, 1989; Muñoz et al., 2004; Miffre et al., 2012; Prata and Prata, 2012), the health impacts of volcanic ash (Horwell and Baxter, 2006; Horwell, 2007), the electrification of volcanic plumes (e.g., James et al., 2000; Miura et al., 2002; Cimarelli et al., 2014) and the meteorological (Durant et al., 2008; Gibbs et al., 2015) and climactic effects of volcanic eruptions (Rampino and Self, 1993; Darteville et al., 2002). As the proportion of particles <0.8 μm cannot be determined with the CX2, characterisation of the ultra-fine GSD is incomplete.

The minimum grain size and image resolution limits of the CX2 also have consequences for the shape measurements. As the DIA approaches the limit of image resolution, the edge detection for particles will be increasingly affected by image pixelation. This could lead to over smoothed or imprecise particle outlines, which will be particularly significant for shape parameters that include particle perimeter (e.g., SPHT; Fig. 5; Liu et al., 2015). Additionally, the shape parameter formulae are not always consistent with other studies, for example, the convexity formulation used by the CX2 software is equivalent to the ‘solidity’ parameter used by Cioni et al. (2014) and Liu et al. (2015). The CX2 is also limited to 2D shape characterisation whereas some studies of volcanic ash compute 3D shape parameters (e.g., sphericity; Ganser, 1993; Dioguardi et al., 2017; Saxby et al., 2018). Whilst it is common that shape parameters have different definitions and formulations, it is not possible to

modify the shape parameter formulations in the CX2 software, meaning that not all shape parameters and formulations can be computed and compared with other shape studies without reanalysing the saved images using other methods.

5.2. Significance of comprehensive grain size characterisation

DIA is a valuable method for scrutinising the size and shape of distal ash samples simultaneously. The median grain size of distal ash deposits is known to stabilise at large distances from source (Fig. 10; Engwell et al., 2014; Engwell and Eychenne, 2016; Cashman and Rust, 2020). The transition to the stable distal grain size occurs when the sedimentation of particles is no longer governed by Stokes law (Engwell and Eychenne, 2016). However, analysis of distal MSH, Mazama and Campanian Ignimbrite tephra shows that the median grain size of distal ash is not uniform across different eruptions, meaning particle ‘size’ alone

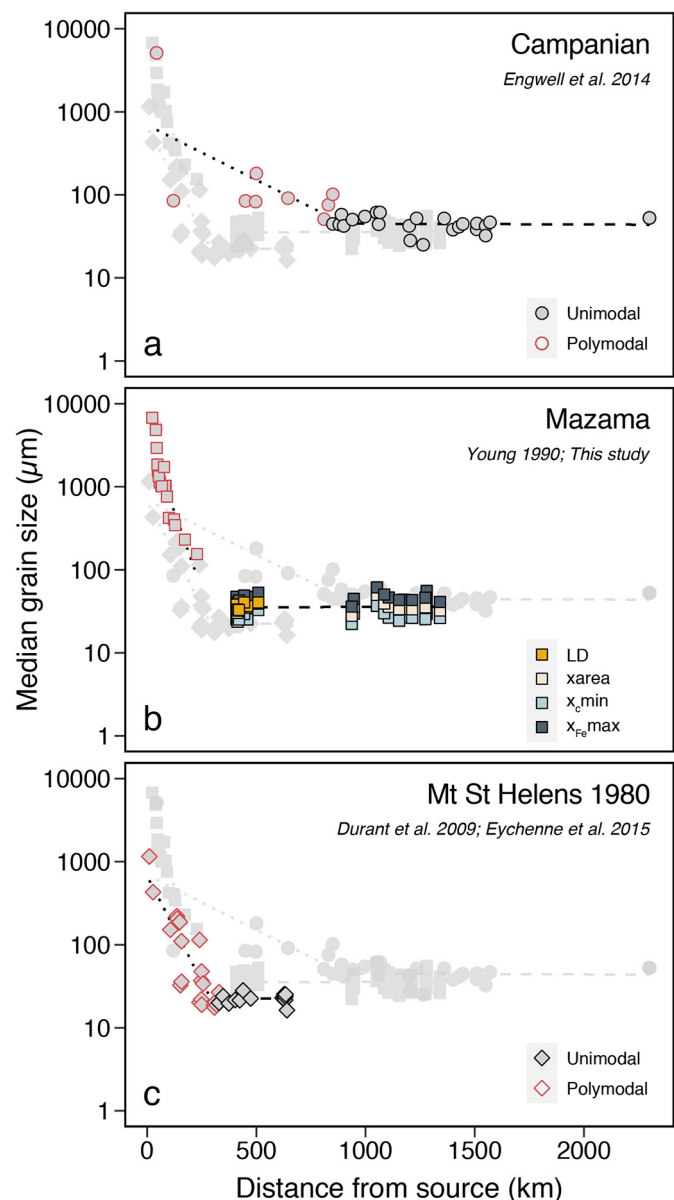


Fig. 10. Grain size of distal tephra with distance from source. a) Campanian tephra with grain size distributions and sub-populations from Engwell et al. (2014). b) Mazama tephra with data from Young (1990), Buckland et al. (2020) and this study. c) Mount St. Helens 1980 data from Durant et al. (2009) and deconvolution by Engwell et al. (2014).

cannot explain this phenomenon (Fig. 10). We propose that differences in how particle size is quantified can partly explain the dissimilar distal grain sizes. For example, the laser diffraction method used to measure the GSD of the Campanian Ignimbrite tephra (Fraunhofer theory; Engwell et al., 2014) produces the equivalent of an $x_{Fe\max}$ distribution (particle long axis), which may explain the apparent coarse distal grain size when compared to GSDs quantified as $x_{c\min}$ (sieving) or x_{area} (laser diffraction using Mie theory).

The inputs used by ash dispersion models, moreover, use a different measure of size than used by physical ash samples. Particle size distributions (PSDs) used by ash dispersion models are specified in terms of equivalent volume sphere diameter (D_v ; Beckett et al., 2015; Saxby et al., 2018). Saxby et al. (2020) used 3D data of ash volumes to demonstrate the divergence between volume-equivalent sphere diameters and long axis ($x_{Fe\max}$) measurements that result from extreme ash morphologies. The 3D data show that for extreme ash shapes the volume equivalent sphere diameter (D_v) is consistently less than the particle long axis (L) as the data plots above the 1:1 line in Fig. 11. For example, for a Campanian Ignimbrite ash shard with an average shard thickness of ~10 µm, the resulting difference between the maximum length (L or $x_{Fe\max}$) and volume equivalent sphere diameter (D_v) is more than 5-fold. Importantly, to quantify particle size as an equivalent volume sphere diameter, 2D image analysis techniques assume that the equivalent area circle diameter (x_{area}) can be converted directly to D_v , although the relation between x_{area} and D_v varies with the 3D shape. These differences partly explain the mismatch between physical measurements of ash shape (GSDs) and the PSDs used in ash dispersion models.

Another explanation for the coarse grain size of the distal Campanian Ignimbrite and Mazama samples relative to the MSH distal tephra is related to particle shape (Fig. 12). Non-spherical particles have higher drag coefficients and lower settling velocities than volume-equivalent spherical particles (Mele et al., 2011; Dioguardi et al., 2017; Saxby et al., 2018, 2019). The low values of SPHT for distal Campanian Ignimbrite ash, for example, reflect the high proportion of glass shards and plates seen in SEM images (Fig. 12b). The higher SPHT values of MSH 1980 tephra, on the other hand, are consistent with SEM images that

show particles that are more elliptical in shape (Fig. 12d). Therefore, it is likely that the differences in the distal grain sizes (Fig. 10) reflect both different parameterisations of size and the impact of particle shape on terminal settling velocities. It is also possible that the differences in distal median grain size reflect the initial fragmentation processes. For instance, the fine-grained MSH ash ($Md \sim 20 \mu m$) has been attributed to the co-PDC plume formed as a result of the lateral blast (Eychenne et al., 2015).

Particle density also governs the settling velocity of tephra. Parallel sieve and CX2 analyses, paired with density measurements, highlight the non-uniform density distribution in coarse Mazama tephras (Fig. 8) and provide a qualitative assessment of density across the size array. Importantly, the density distribution measured for the coarse Mazama samples (Fig. 8c) differs from the sigmoidal distributions of clast density that have been measured and modelled in other tephra deposits (e.g., Barberi et al., 1989; Koyaguchi and Ohno, 2001; Bonadonna and Phillips, 2003; Eychenne and Le Pennec, 2012). The main difference is that the maximum measured density (~2.6 g cm⁻³) exceeds the glass density (~2.1 g cm⁻³), which is often used to approximate the density of the very fine ash that is typically dominated by glass fragments. Whilst the high proportion of lithics and iron titanium oxides in the Mazama tephra contribute to this extreme density value, crystal concentrations are frequently observed in fallout deposits (Taupo, Walker, 1981; MSH, Carey and Sigurdsson, 1982; Santa Maria, Williams and Self, 1983) and it is likely that their occurrence could influence interpretations of GSDs, especially when quantified as mass distributions without reference to parallel componentry analyses. Moreover, componentry is often determined from SEM images (Liu et al., 2017; Buckland et al., 2018; McNamara et al., 2018); without consideration of particle density, the componentry proportions from SEM images do not map directly to the proportion of the sample mass. This has implications for methods that use the proportion of crystals in deposits to calculate erupted volumes (Walker, 1980; Pyle, 1989; Fierstein and Nathenson, 1992; Scarpati et al., 2014). Whilst crystal and lithic concentrations pose a challenge for grain size analysis methods, sample density does converge on the glass density at small grain sizes (distal ash). Understanding where the transition to stable ash density occurs is important for ash

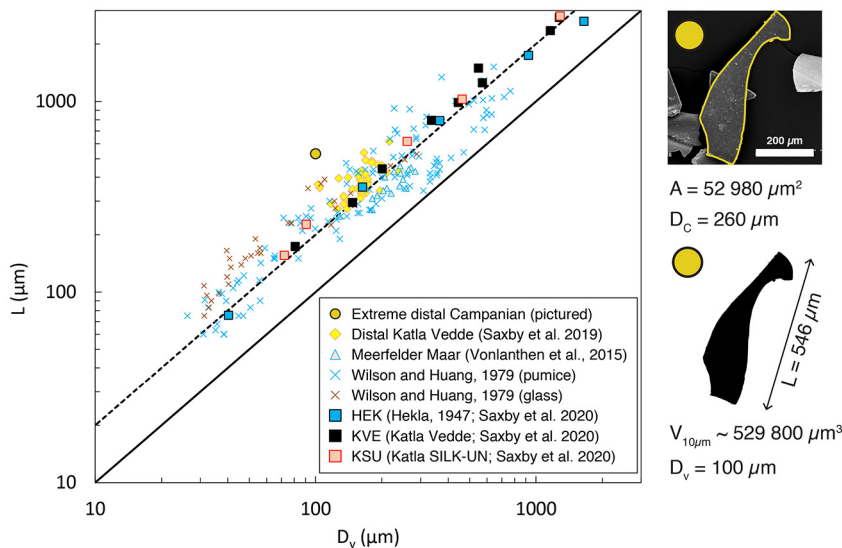


Fig. 11. Volume-equivalent sphere diameter D_v vs long axis length L with example extreme Campanian Ignimbrite ash shard (circle symbol). A is the 2D area of the particle and D_c is the equivalent circle diameter. Square symbols show means (from X-ray CT data, Saxby et al., 2020); diamond symbols are from optical measurements (Saxby et al., 2019) and all other symbols are individual particle measurements collated in Saxby et al. (2020). Solid line: $y = x$, dashed line: $y = 2x$. The SE image (top right) and binary image (bottom right) illustrate how the long axis (L) and equivalent circle diameter (D_c) is determined from 2D image analysis. (Vonlanthen et al., 2015; Wilson and Huang, 1979)

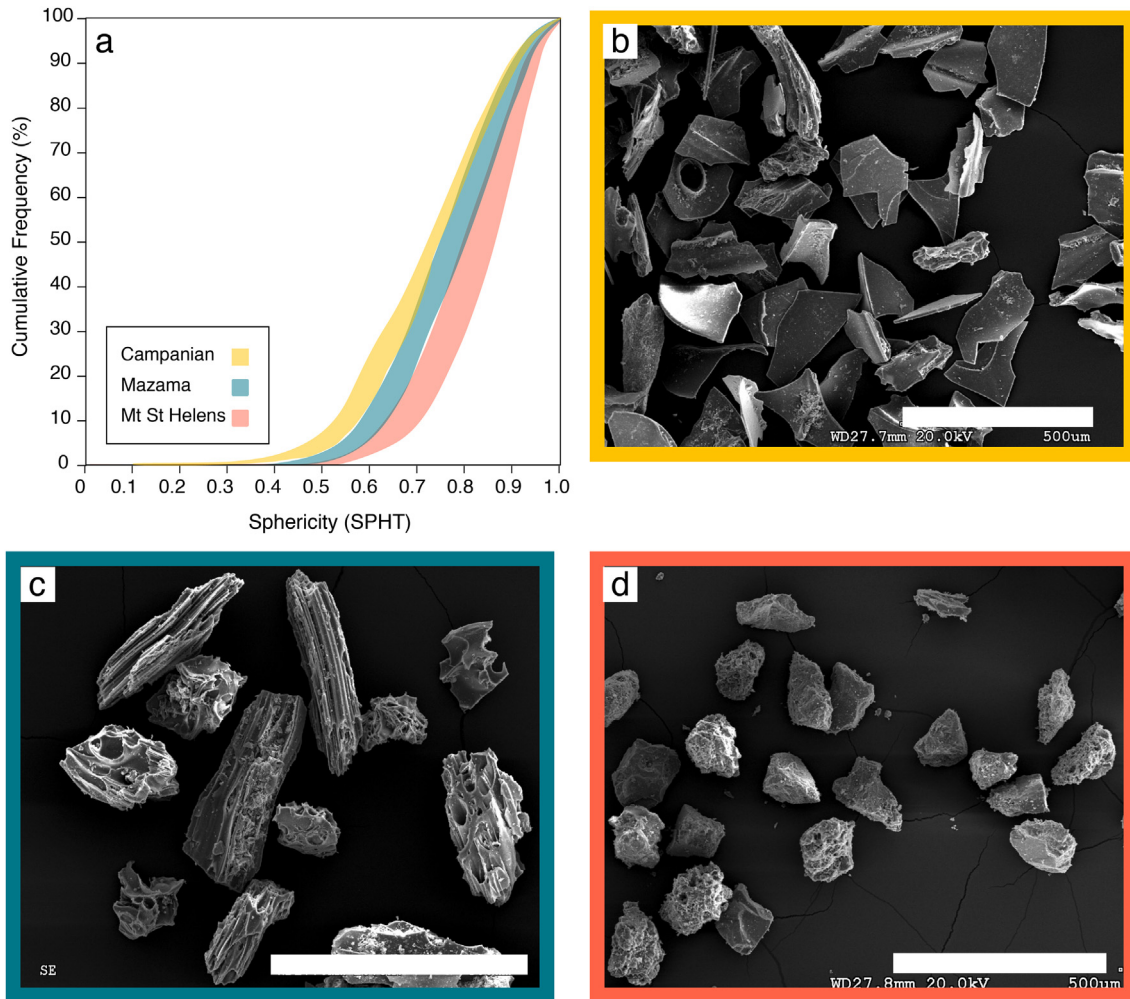


Fig. 12. Sphericity distributions and SE images of distal tephra. Sampling distance ranges: Campanian Ignimbrite ~600–2300 km, Mazama tephra ~400–1350, Mount St. Helens ~150–400 km from source. a) Ranges of multiple individual SPHT distributions for each distal tephra suite. b-d) Images collected on the Hitachi S-3500 N SEM at the University of Bristol in secondary electron mode. Samples were sieved between 90 and 125 μm , mounted on carbon stubs gold coated. Images were collected at 20 kV using a working distance of ~27.7 mm. White bars are 500 μm in all images. Sample name and distance from source: b) Borschevo ~2300 km; c) Andies Prairie (MZ73) 444 km and d) Starbuck (MSH_SB) 314 km (Supplementary S2).

dispersion modelling and likely relates to the eruption intensity and parent magma.

6. Conclusions

Quantifying the size of an irregular shaped particle can be ambiguous and the range of methods available to analyse grain size adds another source of variability to the definition of particle 'size' (Bagheri et al., 2015). The heterogenous nature of tephra, which is often a mixture of components with varied particle densities and shapes, also complicates size analysis. We have shown, however, that dynamic image analysis methods can provide a useful protocol for characterising the size and shape of irregular particles. For example, sieving, which is often considered to sort by size, actually sorts non-spherical particles by size and shape and the size range within a sieve fraction depends on the size parameter used (Sanford and Swift, 1971). In contrast, DIA can measure continuously over a large size range and GSDs can be quantified according to multiple size measures. DIA also quantified GSDs as volume distributions which facilitates comparisons between DIA methods and other techniques such as laser diffraction. Using grain size statistics, we show that both GSDs and the interpretation of GSDs are sensitive to the method of particle size analysis. For example, different sub-populations may be deconvolved from multi-modal deposits that have been analysed in different ways. This suggests that caution

should be used when comparing GSDs and their statistics for samples that have been analysed using different methods. Similarly, associating eruptive processes to grain size sub-populations could be influenced by the starting GSD and the method of deconvolution.

Our analysis shows that the observed discrepancy between PSDs used in volcanic ash dispersion models and ground-based GSDs (Bonadonna et al., 2011; Stevenson et al., 2015) can be explained by a combination of different analysis methods, different size parameterisations, different size ranges and the impact of non-spherical particles. For instance, large distal ash grains often exhibit extreme shapes, that when described using $x_{Fe}max$ or their long axis appear oversized compared to their volume-equivalent sphere diameter (Saxby et al., 2020). Importantly, the disparity in size definitions needs to be considered when comparing model results to deposit data and when using deposit data (GSDs) as the basis for model PSDs. Characterising the 3D morphology of volcanic particles and their density is impractical on a large scale, although this would provide the necessary information to fully resolve the aerodynamic properties of tephra. We have shown however, that 2D methods of size analysis such as DIA can provide insight into the properties of distal ash and that careful consideration of size methods and the impact of non-spherical particles have in part explained the differences between the grain size of distal tephra. This information could be used to inform the PSDs used by ash dispersion models, especially if predicting long range ash dispersal is the main goal.

Data availability

Datasets related to this article can be found in the supplementary material.

Declaration of Competing Interest

The authors declare that they have no known competing financial interests or personal relationships that could have appeared to influence the work reported in this paper.

Acknowledgements

H.M.B is supported by a NERC GW4+ Doctoral Training Partnership studentship from the Natural Environment Research Council (NERC;

NE/L002434/1) with additional support from the British Geological Survey. J.S. was supported by NERC (NE/M010384/1) and the Met Office, UK (CASE studentship P100339). S.L.E. publishes with permission of the CEO, British Geological Survey. K.C. acknowledges an AXA Research Fund and a Royal Society Wolfson Merit Award. We would like to thank those who shared their samples with us: E. Liu (Hverfjall Fires); U. Mueller (CI, Tenaghi Phillipon), W. Ferrand (CI, Franchi Cave), D. Pyle (CI, Russia), D. Veres (CI, Romanian Loess); B. Carson (MSH); B. Jensen (Mazama, Canada). Additional thanks go to H. Goodes who helped setup and run the CX2 in the School of Earth Sciences at the University of Bristol. We extend further thanks to A. Durant and J. Eychenne for sharing their grain size data and distribution analyses of the MSH samples. Finally, we thank T. Giachetti and J. Castro for their insightful reviews that improved the paper and K. Russell for quick and helpful editorial handling.

Appendix A. Review of grain size methods in volcanology

A.1. Coarse sieving

The GSD of coarse ($>125 \mu\text{m}$) unconsolidated tephra is typically measured by sieving. The tephra is passed through a series of nested sieves where the aperture size typically decreases on the logarithmic φ or Krumbein scale (Krumbein, 1934) in whole- φ , half- φ or quarter- φ increments where

$$\varphi = -\log_2 d \quad (\text{A.1})$$

and d is the length of the side of the square aperture in mm. The φ -scale is widely used in sedimentology and volcanology instead of an arithmetic or linear scale to avoid emphasis of this mass-based measure on the coarse sediment (Blott and Pye, 2001). Manual or mechanical shaking, with or without the addition of water, is used to segregate the tephra into the individual sieve fractions. The minimum particle 'size' (diameter for a sphere) within a sieve fraction is equal to d . The GSD is then reported as the percentage of the analysed mass (weight percent) retained in each sieve fraction. Sieving is a low cost and established method that is often the only available tool for measuring very coarse size fractions particularly whilst in the field (Folk and Ward, 1957; Walker, 1971; Fairbridge and Joanne, 1978). However, sieving does have limitations. Firstly, the sieve size is only equal to the particle size for spheres. Anisotropic particle shapes mean that clasts do not always pass through the sieve mesh according to the same dimension. For example, flat or elongated particles can be sorted according to their largest or smallest dimension which can vary substantially (e.g., needle like particles in Katla SILK layers; Saxby et al., 2018, 2020). This means that sieving sorts by both size and shape (Komar and Cui, 1984). Agitation of delicate tephra when sieving can also lead to clast breakage and alteration of the GSD and particle shape during analysis (Cox et al., 2017) so the reproducibility of the GSD depends on the method and duration of agitation. The amount of material sieved affects the ease of GSD measurement, particularly for coarse material where large quantities of material are required to ensure a representative aliquot (Swineford and Swineford, 1946; Sarocchi et al., 2011; Román-Sierra et al., 2013). Interpretations of GSDs produced by sieving also depend on the sieve interval. Ideally, sieve intervals should be quarter- or half- φ , because larger intervals present difficulties in computing statistics, especially for fractions $>2 \text{ mm}$ (-1φ ; Hails et al., 1973). The grain size range typically covered by sieves is from $\sim 125 \text{ mm}$ to $20 \mu\text{m}$ (Table 1). However, sieving below $\sim 125 \mu\text{m}$ is challenging as fine sieves are prone to overloading, and fine material can form coarser aggregates or loft when agitated meaning that the particles do not pass into the correct sieve fraction and can be lost. For this reason, other methods are preferred for measuring particles $<125 \mu\text{m}$.

A.2. Particle sedimentation

An alternative method of grain size analysis uses rates of particle sedimentation; this method measures the velocities of particles settling in a fluid of known viscosity and density and can cover a wide range of particle sizes ($\sim 50\text{--}5000 \mu\text{m}$; Table 1; Gibbs et al., 1971). From the measured settling velocities, the diameters of dense equivalent spheres that would have the same settling velocities are calculated using an empirical equation (Gibbs et al., 1971). A variant is the pipette method, which uses water as the fluid and has been used with volcanic tephra (Watanabe et al., 1999; Wiesner et al., 2004). Another sedimentation method is the Roller apparatus (Roller, 1931; Riley et al., 2003), an air elutriation device that separates particles according to their settling velocities in air. As with sieving, however, sedimentation methods of grain size analysis indirectly measure the effects of grain shape, and specifically for these methods, variations in particle density (Sanford and Swift, 1971; Komar and Cui, 1984; Beuselinck et al., 1998). Moreover, the settling behaviour of fine material ($<125 \mu\text{m}$) is poorly described by existing settling laws because of aggregation, Brownian motion ($<10 \mu\text{m}$) and complex flow and depositional regimes (Rose and Durant, 2009; Brown et al., 2012; Engwell and Eychenne, 2016; Saxby et al., 2018).

A.3. Laser diffraction

Laser diffraction is the most common method used in volcanology to characterise the GSD of fine material (e.g., Horwell, 2007; Buckland et al., 2018; Genareau et al., 2019). The sample is dispersed in a liquid (commonly distilled water) to form a suspension that passes by three lasers with different wavelengths. The diffraction of the laser beams by the suspended particles is used to calculate particle size by inverting the measured scattering pattern. The GSD is then output as a volume distribution; combining laser diffraction data with sieve data thus requires estimates of particle density. This method is rapid ($<2 \text{ min per analysis}$) and instruments such as the Mastersizer 3000 by Malvern Panalytical (formerly Malvern Instruments Ltd) can measure a particle size range of $0.01\text{--}3500 \mu\text{m}$ (Malvern Panalytical, 2020). However, the mathematical model chosen to resolve the laser scattering can introduce errors. For example, Mie scattering theory assumes spherical particles and requires an assumption of refractive index. Tephra is very rarely close to spherical, however, and the refractive index is not routinely measured. Moreover, as tephra is commonly a mixture of crystals, lithics and glass, one refractive index will not be representative of the whole sample. An alternative mathematical model used to resolve the laser scattering is the Fraunhofer theory, which assumes particles are flat discs and that the particles only cause diffraction, thus it does not require an assumption of refractive index (Beuselinck et al., 1998; Cyr and Tagnit-Hamou, 2001). However, the Fraunhofer approximation can overestimate the proportion of very fine particles ($<10 \mu\text{m}$) due to this simplification (Cyr and Tagnit-Hamou, 2001).

A.4. Electrozone sensing

Another method of characterising the GSD of fine material is electrozone sensing, or the Coulter counter method, which has a measurement range of ~0.4–1600 µm. This requires that particles are suspended in an electrically conductive fluid. The suspended particles are counted as they pass through an aperture of known diameter which generates a pulse in electrical resistivity that is measured and related to an equivalent sphere diameter based on the calibration curve of the instrument (Figueiredo, 2006). The resulting GSD can be output either as a number (particle count) or volume (converted from equivalent sphere diameter) distribution. This method has been used to measure the GSD of volcanic ash (e.g., Sparks et al., 1983; Carey et al., 1988; Brand et al., 2016) and has the benefit of being non-optical and therefore not affected by variations in particle opacity or reflectivity. However, similar to particle sedimentation methods, electrozone sensing methods quantify size as an equivalent sphere diameter and provide no information about particle shape.

A.5. Grain size analysis from image analysis

Image analysis is a flexible method for characterising the grain size and shape of coarse- and fine-grained materials. Here we focus on the application of image analysis to determine the GSD for fine-grained materials, but there are a number of studies that use image analysis to determine the GSD of coarse and consolidated volcanic material (e.g., Capaccioni et al., 1997; Sarocchi et al., 2011; Jutzeler et al., 2012). The grain size of fine ash can be characterised using scanning electron microscope (SEM) images, most commonly collected in secondary electron mode (e.g., Horwell et al., 2003; Riley et al., 2003; Coltell et al., 2008; Liu et al., 2015). This method allows simultaneous classification of particle shape and componentry (lithic, glass or crystal). However, particle imaging using the SEM may require some sample preparation, such as sieving, to ensure the particles are imaged at the optimal resolution. Furthermore, large particles may be underrepresented if small sample volumes are used. There is also an assumption of 3D shape required to convert from 2D images to a GSD in terms of volume % (Sahagian and Proussevitch, 1998). Whilst SEM methods can provide excellent particle information, such as shape and the proportion of different components, the time required for these analyses (~hours to days) exceeds that of other methods such as laser diffraction (~minutes per analysis). This may be a disadvantage for some applications of grain size data, for example, if being analysed for rapid assessments of tephra hazard during an eruption.

Other image analysis methods use optical imagery. For example, the Morphologi G3 particle analyser by Malvern Panalytical scans and rapidly images particles that have been dispersed onto a glass plate; size and shape are measured using the built-in software. Similar to SEM analyses, this method requires that the sample is sieved prior to analysis to ensure optimal particle dispersion and image resolution (Leibrandt and Le Pennec, 2015; Buckland et al., 2018; Freret-Lorgeril et al., 2019). Studies of cryptotephra (non-visible tephra layers) also quantify grain size using optical imaging methods; size is typically measured along the longest particle axis (e.g., Palais et al., 1992; Zdanowicz et al., 1999; Stevenson et al., 2015). Here chemical and physical tephra extraction (Dugmore and Newton, 1992; Cooper et al., 2019) is required before tephra shards are counted and imaged using an optical microscope. However, part of the tephra extraction process involves removing very fine material by wet sieving (<20 µm) and only a small number of particles are measured (~100; Stevenson et al., 2015). These aspects of the sample handling, combined with the different size parameterisation, make cryptotephra GSDs difficult to compare with GSDs from other methods (Cashman and Rust, 2020).

A.6. In situ methods

In situ methods of particle size analysis utilise a variety of the measurement principles used by laboratory methods such as diffraction and image analysis (Table 1). As with laboratory methods of size analysis, the grain size range and definition of size is unique to each in situ method and instrument. Ground-based radar systems such as the PLUDIX instrument (Scollo et al., 2005; Bonadonna et al., 2011) measure the settling velocity of particles from ~1000–10,000 µm. The settling velocity is converted into a PSD by assuming spheres with variable densities (Bonadonna et al., 2011); thus size is quantified as an equivalent sphere diameter. Optical disdrometers, such as the Parsivel², also quantify size as the volume equivalent sphere diameter according to the manufacturers specifications (Kozono et al., 2019; OTT, 2020), however, studies of rainfall found that the measured size of non-spherical particles is closer to the maximum horizontal diameter (Table 1; Adachi et al., 2013). In situ high resolution 2D imaging of active tephra fall can measure particles from 62 to 2000 µm; the images can be used to determine multiple size descriptors including minimum and maximum particle lengths and area equivalent measures (Miwa et al., 2020). Finally, the methods used to determine PSDs from satellite infrared measurements typically assume that the particles are dense spheres with a constant refractive index and that the scattering can be resolved using Mie theory; thus the 'size' reported refers to a sphere diameter (Wen and Rose, 1994; Pavolonis et al., 2013; Kylling et al., 2014; Stevenson et al., 2015).

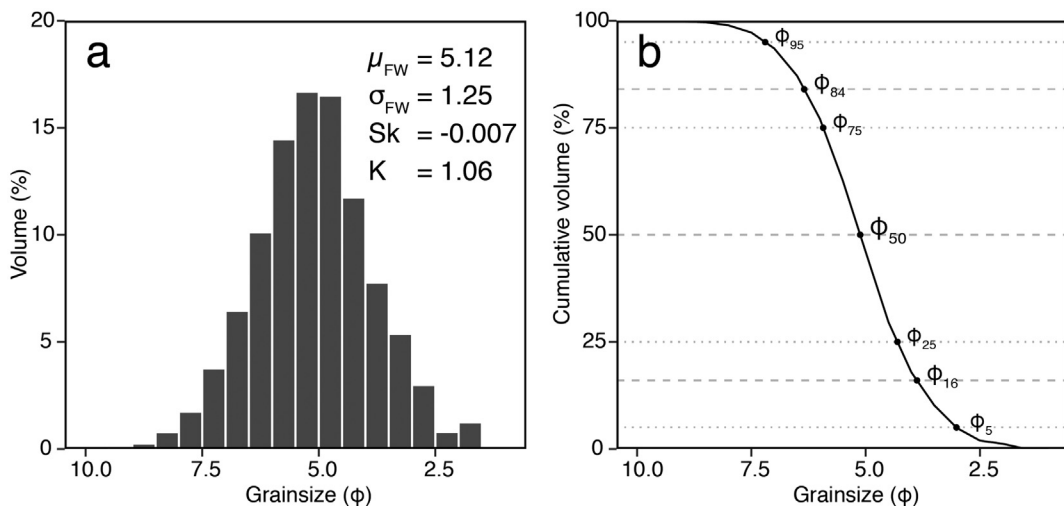


Fig. B1. Example of the FW parameters calculated for distal Mazama sample AP1. a) The grain size distribution measured using the CX2 quantified as the volume percent in each half- ϕ size fraction. b) Cumulative grain size distribution represented as the percentage coarser than the nominal grain size fraction with the interpolated values required for calculating the FW statistics plotted as black circles.

2015). Note that the term 'effective radius' that is used in remote sensing refers to a log-normal PSD that contains a range of particle sizes rather than a single particle size (Stevenson et al., 2015).

Appendix B. Grain size statistics and distribution fitting

B.1. Definitions of parameters and probability density functions

The Folk and Ward (1957) graphical statistics are calculated using interpolated values from the cumulative distribution function (Fig. B1b). The parameters are calculated using the formulas below:

$$\mu_{FW} = \frac{\varphi_{16} + \varphi_{50} + \varphi_{84}}{3} \quad (\text{B.1})$$

$$\sigma_{FW} = \frac{\varphi_{84} - \varphi_{16}}{4} + \frac{\varphi_{95} + \varphi_5}{6.6} \quad (\text{B.2})$$

$$Sk = \frac{\varphi_{16} + \varphi_{84} - 2\varphi_{50}}{2(\varphi_{84} - \varphi_{16})} + \frac{\varphi_5 + \varphi_{95} - 2\varphi_{50}}{2(\varphi_{95} - \varphi_5)} \quad (\text{B.3})$$

$$K = \frac{\varphi_{95} - \varphi_5}{2.44(\varphi_{75} - \varphi_{25})} \quad (\text{B.4})$$

where μ_{FW} denotes the Folk and Ward mean, σ_{FW} is the standard deviation or sorting, Sk is the skewness and K is Kurtosis. φ_y is the value in φ where y denotes the percentile of the cumulative distribution, e.g., φ_{50} is the median grain size (Fig. B1b). The values of sorting, skewness and Kurtosis then correspond to a qualitative classification according to the categories in Table B1.

Table B1

Descriptive terminology corresponding to the Folk and Ward parameters calculated for grain size data on the φ scale.

Sorting (σ_{FW})		Skewness (Sk)		Kurtosis (K)	
Very well sorted	<0.35	Very fine skewed	+0.3 to +1.0	Very platykurtic	<0.67
Well sorted	0.35–0.50	Fine skewed	+0.1 to +0.3	Platykurtic	0.67–0.90
Moderately well sorted	0.50–0.70	Symmetrical	+0.1 to –0.1	Mesokurtic	0.90–1.11
Moderately sorted	0.70–1.00	Coarse skewed	–0.1 to –0.3	Leptokurtic	1.11–1.50
Poorly sorted	1.00–2.00	Very coarse skewed	–0.3 to –1.0	Very leptokurtic	1.50–3.00
Very poorly sorted	2.00–4.00			Extremely leptokurtic	>3.00
Extremely poorly sorted	>4.00				

FW parameters assume that the GSD is log-normally distributed (normal on the φ -scale). However, GSDs can also be fit to probability density functions (PDFs) directly. When working with grain size data on the φ scale the GSD can be fit using a normal distribution which has the PDF:

$$f_{norm}(\varphi) = \frac{1}{\sigma_\varphi \sqrt{2\pi}} \exp \left[-\frac{1}{2} \left(\frac{\varphi - \mu_\varphi}{\sigma_\varphi} \right)^2 \right] \quad (\text{B.5})$$

where φ is the grain size in φ units, μ_φ denotes the mean and σ_φ is the standard deviation. This can be extended to facilitate the fitting of mixture models where the PDF is described as the sum of multiple normal distributions multiplied by their mixing proportion. For example, the PDF for a bimodal distribution which is the sum of two normal distributions is:

$$f_{bi-norm}(\varphi) = p_1 \frac{1}{\sigma_{\varphi 1} \sqrt{2\pi}} \exp \left[-\frac{1}{2} \left(\frac{\varphi - \mu_{\varphi 1}}{\sigma_{\varphi 1}} \right)^2 \right] + p_2 \frac{1}{\sigma_{\varphi 2} \sqrt{2\pi}} \exp \left[-\frac{1}{2} \left(\frac{\varphi - \mu_{\varphi 2}}{\sigma_{\varphi 2}} \right)^2 \right] \quad (\text{B.6})$$

where p_1 and p_2 are the mixing proportions of each population. When fitting a normal distribution to GSDs on the φ -scale, it must be remembered that the mean and standard deviation relate to the logarithm of the data and that the GSD is log-normal in linear space. This is an important distinction because when data follows a log-normal distribution the mean, mode and median are not equal. Furthermore, data visualisation of GSDs on the φ -scale can be distorted (Fig. B1a).

It can be preferable to fit log-normal PDFs directly to grain size data and to work in metric units as is standard procedure in engineering and aerosol science (Darteville et al., 2002). To fit a log-normal function, the grain size data cannot be on the φ -scale because d must be greater than 0 (Eq. B7). Therefore, the GSD must either be output using a linear bin configuration or exponentiated from the φ scale ($d = 2^{-\varphi}$). The PDF of a log-normal distribution is:

$$f_{lnorm}(d) = \frac{1}{d\sigma' \sqrt{2\pi}} \exp \left[-\frac{(\ln(d) - \mu')^2}{2\sigma'^2} \right] \text{ for } d > 0 \quad (\text{B.7})$$

where d is the grain size in mm, μ' denotes the mean of the natural logarithm of the data and σ' is the standard deviation of the natural logarithm of the data. Using these parameters, the mean (μ), median (M_d) and mode (M_0) can also then be calculated:

$$\mu_L = \exp \left[\mu' + \frac{1}{2} \sigma'^2 \right] \quad (\text{B.8})$$

$$M_d = \exp[\mu'] \quad (\text{B.9})$$

$$Mo_L = \exp [\mu' - \sigma'^2] \quad (B.10)$$

where the μ_L is the mean, Md_L is the median and Mo_L is the mode of the log-normal distribution in mm units. Mixture models of log-normal distributions can also be used to describe GSDs where the PDF is the sum of the PDF of each sub-population multiplied by the mixing proportion:

$$f_{bi-\lnorm}(d) = p_1 \frac{1}{d\sigma'_1 \sqrt{2\pi}} \exp \left[-\left(\frac{\ln(d) - \mu'_1}{2\sigma'^2_1} \right)^2 \right] + p_2 \frac{1}{d\sigma'_2 \sqrt{2\pi}} \exp \left[-\left(\frac{\ln(d) - \mu'_2}{2\sigma'^2_2} \right)^2 \right] \quad (B.11)$$

Grain size distributions can also be described using a Weibull distribution which has the PDF:

$$f_{Weibull}(d) = \frac{k}{\lambda} \left(\frac{d}{\lambda} \right)^{k-1} \exp \left[-\left(\frac{d}{\lambda} \right)^k \right] \text{ for } d \geq 0 \quad (B.12)$$

where d is particle diameter in mm, k is the shape parameter and λ is the scale parameter. Similar to the log-normal distribution, the Weibull distribution cannot be fit to grain size data on the ϕ -scale so the GSD must be quantified in mm. GSDs can also be fit with mixtures of Weibull PDF, for example the PDF of a bimodal Weibull distribution is:

$$f_{bi-Weibull}(d) = p_1 \frac{k_1}{\lambda_1} \left(\frac{d}{\lambda_1} \right)^{k_1-1} \exp \left[-\left(\frac{d}{\lambda_1} \right)^{k_1} \right] + p_2 \frac{k_2}{\lambda_2} \left(\frac{d}{\lambda_2} \right)^{k_2-1} \exp \left[-\left(\frac{d}{\lambda_2} \right)^{k_2} \right] \quad (B.13)$$

where p_1 and p_2 are the mixing proportions, k_1 and k_2 are the scale parameters, and λ_1 and λ_2 are the scale parameters.

The mean, median and mode of the Weibull distribution can be calculated from the shape and scale parameters using the equations:

$$\mu_W = \lambda \cdot \Gamma \left(\frac{1}{k} + 1 \right) \quad (B.14)$$

$$Md_W = \lambda (\ln 2)^{\frac{1}{k}} \quad (B.15)$$

$$Mo_W = \lambda \left(1 - \frac{1}{k} \right)^{\frac{1}{k}} \quad (B.16)$$

where the μ_W is the mean, Γ is the gamma function, Md_W is the median and Mo_W is the mode in mm units.

B.2. Methods of fitting distributions

GSDs are reported as histograms, in other words, the individual particle sizes are not known the proportion of the total mass or volume of particles is known within a grain size range. This is why graphical parameters and the method of moments have been favoured (Folk and Ward, 1957; Blott and Pye, 2001) as they can be easily calculated from binned data. An alternative approach is to find the best fit parameters of a chosen function (e.g., log-normal or Weibull) using least squares regression, typically by fitting the cumulative density function (e.g., Macias Garcia et al., 2004). Another method is to simulate measurements of individual particle sizes based on the proportion within each grain size bin, which facilitates the use of maximum likelihood estimation methods.

For this contribution we have used the latter approach of simulating data based on the measured GSD (Fig. B2). We chose this approach because we found that the least squares regression approach was more sensitive to the grain size bin configuration than maximum likelihood estimates. We simulate the grain size data by assuming that the weight or volume percent within each grain size bin is equivalent to the number or frequency of measurements (n). We then generate a uniform distribution of grain size measurements, where the number of measurements is equal to m and the absolute value ranges between the minimum and maximum size of the bin. This simulated dataset can then be used to fit a range of PDFs.

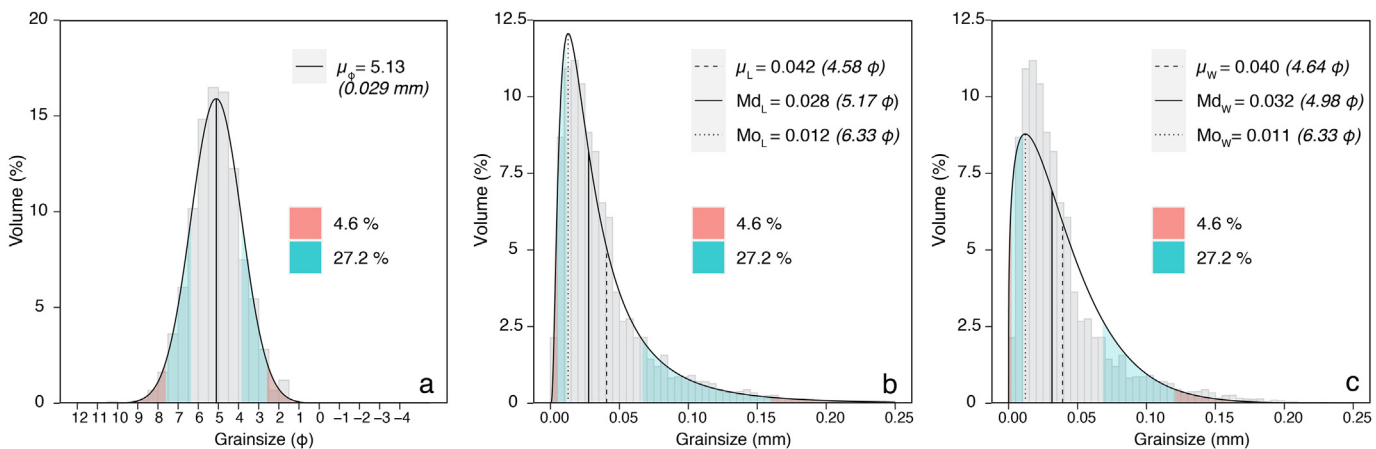


Fig. B2. Simulated grain size data for distal Mazama sample AP1 fit with a) normal; b) log-normal and c) Weibull probability density functions. The coloured segments correspond to >1 standard deviation, so the blue shaded area contains 27.2% of the distribution (± 1 to 2σ) and the red shaded area contains 4.6% of the distribution ($>2\sigma$).

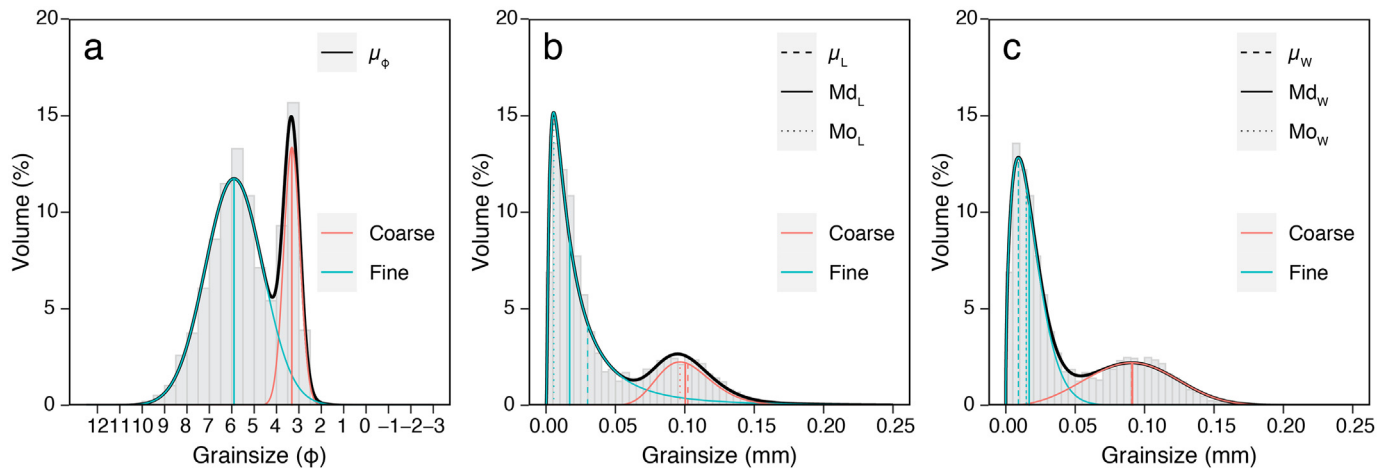


Fig. B3. Simulated grain size data for distal Mount St Helens sample SB fit with bimodal a) normal; b) log-normal and c) Weibull probability density functions. The coarse and fine sub-populations are indicated by the coloured PDFs with the mode, mean and median of each population also indicated by corresponding lines. The solid black line is the bimodal distribution according to Eqs. B6, 11 and 13.

We fit log-normal and Weibull distributions to the simulated data using the ‘fitdistrplus’ package in R (Delignette-Muller and Dutang, 2015). An example of a normal, log-normal and Weibull distribution fit to a unimodal grain size distribution (distal Mazama) is shown in Fig. B2. We fit bimodal distributions using the ‘mixfit’ function from the ‘mixR’ R package (Yu, 2018) with example fits shown in Fig. B3 (distal MSH).

In the main text, we report the FW parameters and the parameters of bimodal normal distributions fit to data on the ϕ -scale (Eq. B6) to allow comparisons with previously published grain size statistics. This also avoids any confusion that might arise from comparing Weibull parameters determined by different fitting methods (e.g., DECOLOG; Eychenne et al., 2015).

Appendix C. Supplementary data

Supplementary data to this article can be found online at <https://doi.org/10.1016/j.jvolgeores.2021.107257>.

References

- Adachi, A., Kobayashi, T., Yamauchi, H., Onogi, S., 2013. Detection of potentially hazardous convective clouds with a dual-polarized C-band radar. *Atmosph. Meas. Techniq. Discussions* 6.
- Alfano, F., Bonadonna, C., Watt, S., Connor, C., Volentik, A., Pyle, D.M., 2016. Reconstruction of total grain size distribution of the climatic phase of a long-lasting eruption: the example of the 2008–2013 Chaitén eruption. *Bull. Volcanol.* 78, 46. <https://doi.org/10.1007/s00445-016-1040-5>.
- Bagheri, G.H., Bonadonna, C., Manzella, I., Vonlanthen, P., 2015. On the characterization of size and shape of irregular particles. *Powder Technol.* 270, 141–153. <https://doi.org/10.1016/j.powtec.2014.10.015>.
- Barberi, F., Cioni, R., Rosi, M., Santacroce, R., Sbrana, A., Vecchi, R., 1989. Magmatic and phreatomagmatic phases in explosive eruptions of Vesuvius as deduced by grain-size and component analysis of the pyroclastic deposits. *J. Volcanol. Geotherm. Res.* 38, 287–307. [https://doi.org/10.1016/0377-0273\(89\)90044-9](https://doi.org/10.1016/0377-0273(89)90044-9).
- Bebbington, M., Cronin, S.J., Chapman, I., Turner, M.B., 2008. Quantifying volcanic ash fall hazard to electricity infrastructure. *J. Volcanol. Geothermal Res., Volcanic Flows and Falls* 177, 1055–1062. <https://doi.org/10.1016/j.jvolgeores.2008.07.023>.
- Beckett, F.M., Witham, C.S., Hort, M.C., Stevenson, J.A., Bonadonna, C., Millington, S.C., 2015. Sensitivity of dispersion model forecasts of volcanic ash clouds to the physical characteristics of the particles. *J. Geophys. Res.-Atmos.* 120, 11,636–11,652. <https://doi.org/10.1002/2015JD023609>.
- Beuselinck, L., Govers, G., Poesen, J., Degraer, G., Froyen, L., 1998. Grain-size analysis by laser diffractometry: comparison with the sieve-pipette method. *CATENA* 32, 193–208. [https://doi.org/10.1016/S0341-8162\(98\)00051-4](https://doi.org/10.1016/S0341-8162(98)00051-4).
- Blake, D.M., Wilson, T.M., Cole, J.W., Deligne, N.I., Lindsay, J.M., 2017. Impact of volcanic ash on road and airfield surface skid resistance. *Sustainability* 9, 1389. <https://doi.org/10.3390/su9081389>.
- Blott, S.J., Pye, K., 2001. GRADISTAT: a grain size distribution and statistics package for the analysis of unconsolidated sediments. *Earth Surf. Process. Landf.* 26, 1237–1248. <https://doi.org/10.1002/esp.261>.
- Bonadonna, C., Houghton, B.F., 2005. Total grain-size distribution and volume of tephra-fall deposits. *Bull. Volcanol.* 67, 441–456. <https://doi.org/10.1007/s00445-004-0386-2>.
- Bonadonna, C., Phillips, J.C., 2003. Sedimentation from strong volcanic plumes. *J. Geophys. Res. Solid Earth* 108. <https://doi.org/10.1029/2002JB002034>.
- Bonadonna, C., Genco, R., Gouhier, M., Pistolesi, M., Cioni, R., Alfano, F., Hoskuldsson, A., Rippey, M., 2011. Tephra sedimentation during the 2010 Eyjafjallajökull eruption (Iceland) from deposit, radar, and satellite observations. *J. Geophys. Res. Solid Earth* 116. <https://doi.org/10.1029/2011JB008462>.
- Bonadonna, C., Folch, A., Loughlin, S., Puempel, H., 2012. Future developments in modelling and monitoring of volcanic ash clouds: outcomes from the first IAVCEI-WMO workshop on Ash Dispersal Forecast and Civil Aviation. *Bull. Volcanol.* 74, 1–10.
- Bonadonna, C., Cioni, R., Pistolesi, M., Connor, C., Scollo, S., Pioli, L., Rosi, M., 2013. Determination of the largest clast sizes of tephra deposits for the characterization of explosive eruptions: a study of the IAVCEI commission on tephra hazard modelling. *Bull. Volcanol.* 75, 680. <https://doi.org/10.1007/s00445-012-0680-3>.
- Brand, B.D., Bendaña, S., Self, S., Pollock, N., 2016. Topographic controls on pyroclastic density current dynamics: Insight from 18 May 1980 deposits at Mount St. Helens, Washington (USA). *J. Volcanol. Geotherm. Res.* 321, 1–17. <https://doi.org/10.1016/j.jvolgeores.2016.04.018>.
- Brown, W.K., Wohletz, K.H., 1995. Derivation of the Weibull distribution based on physical principles and its connection to the Rosin-Rammler and lognormal distributions. *J. Appl. Phys.* 78, 2758–2763. <https://doi.org/10.1063/1.360073>.
- Brown, R.J., Bonadonna, C., Durant, A.J., 2012. A review of volcanic ash aggregation. *Phys. Chem. Earth, Parts A/B/C* 45, 65–78.
- Buckland, H.M., Eychenne, J., Rust, A.C., Cashman, K.V., 2018. Relating the physical properties of volcanic rocks to the characteristics of ash generated by experimental abrasion. *J. Volcanol. Geotherm. Res.* 349, 335–350. <https://doi.org/10.1016/j.jvolgeores.2017.11.017>.
- Buckland, H.M., Cashman, K.V., Engwell, S.L., Rust, A.C., 2020. Sources of uncertainty in the Mazama isopachs and the implications for interpreting distal tephra deposits from large magnitude eruptions. *Bull. Volcanol.* 82, 23. <https://doi.org/10.1007/s00445-020-1362-1>.
- Burden, R.E., Phillips, J.C., Hincks, T.K., 2011. Estimating volcanic plume heights from depositional clast size. *J. Geophys. Res. Solid Earth* 116. <https://doi.org/10.1029/2011JB008548>.
- Capaccioni, B., Valentini, L., Rocchi, M.B.L., Nappi, G., Sarocchini, D., 1997. Image analysis and circular statistics for shape-fabric analysis: applications to lithified ignimbrites. *Bull. Volcanol.* 58, 501–514. <https://doi.org/10.1007/s004450050158>.
- Carey, S.N., Sigurdsson, H., 1982. Influence of particle aggregation on deposition of distal tephra from the May 18, 1980, eruption of Mount St. Helens volcano. *J. Geophys. Res. Solid Earth* 87, 7061–7072. <https://doi.org/10.1029/JB087B03p07061>.
- Carey, S., Sparks, R., 1986. Quantitative models of the fallout and dispersal of tephra from volcanic eruption columns. *Bull. Volcanol.* 48, 109–125.
- Carey, S.N., Sigurdsson, H., Sparks, R.S.J., 1988. Experimental studies of particle-laden plumes. *J. Geophys. Res. Solid Earth* 93, 15314–15328. <https://doi.org/10.1029/JB093B12p15314>.
- Casadevall, T.J., 1994. The 1989–1990 eruption of Redoubt Volcano, Alaska: impacts on aircraft operations. *J. Volcanol. and Geothermal Res., The 1989–1990 Eruptions of Redoubt Volcano, Alaska* 62, 301–316. [https://doi.org/10.1016/0377-0273\(94\)90038-8](https://doi.org/10.1016/0377-0273(94)90038-8).

- Cashman, K.V., Rust, A.C., 2020. Far-travelled ash in past and future eruptions: combining tephrochronology with volcanic studies. *J. Quat. Sci.* 35, 11–22. <https://doi.org/10.1002/jqs.3159>.
- Castro, M.D.L., Andronico, D., 2008. *Operazioni di base per la misura della distribuzione granulometrica di particelle vulcaniche tramite il CAMSIZER* (Rapporti Tecnici No. 79). Instituto Nazionale di Geofisica e Vulcanologia, Catania.
- Cimarelli, C., Alatorre-Ibargüenotia, M.A., Kueppers, U., Scheu, B., Dingwell, D.B., 2014. Experimental generation of volcanic lightning. *Geology* 42, 79–82. <https://doi.org/10.1130/C34802.1>.
- Cioni, R., Pistolesi, M., Bertagnini, A., Bonadonna, C., Höskuldsson, A., Scateni, B., 2014. Insights into the dynamics and evolution of the 2010 Eyjafjallajökull summit eruption (Iceland) provided by volcanic ash textures. *Earth Planet. Sci. Lett.* 394, 111–123. <https://doi.org/10.1016/j.epsl.2014.02.051>.
- Coltellini, M., Miraglia, L., Scollo, S., 2008. Characterization of shape and terminal velocity of tephra particles erupted during the 2002 eruption of Etna volcano, Italy. *Bull. Volcanol.* 70, 1103–1112. <https://doi.org/10.1007/s00445-007-0192-8>.
- Cooper, C.L., Savov, I.P., Swindles, G.T., 2019. Standard chemical-based tephra extraction methods significantly alter the geochemistry of volcanic glass shards. *J. Quat. Sci.* 34, 697–707. <https://doi.org/10.1002/jqs.3169>.
- Costa, A., Pioli, L., Bonadonna, C., 2016. Assessing tephra total grain-size distribution: Insights from field data analysis. *Earth Planet. Sci. Lett.* 443, 90–107. <https://doi.org/10.1016/j.epsl.2016.02.040>.
- Cox, L., Wood, J., Fan, J., Huang, Y., 2017. *Experimental Separation of Non-spherical Ash Particles by Terminal Velocity* (Master of Engineering). University of Bristol.
- Cyr, M., Tagnit-Hamou, A., 2001. Particle size distribution of fine powders by LASER diffraction spectrometry. Case of cementitious materials. *Mater. Struct.* 34, 342–350. <https://doi.org/10.1007/BF02486485>.
- Dartevelle, S., Ernst, G.G.J., Stix, J., Bernard, A., 2002. Origin of the Mount Pinatubo climactic eruption cloud: Implications for volcanic hazards and atmospheric impacts. *Geology* 30, 663–666. [https://doi.org/10.1130/0091-7613\(2002\)030<0663:OOTMPC>2.0.CO;2](https://doi.org/10.1130/0091-7613(2002)030<0663:OOTMPC>2.0.CO;2).
- Delignette-Muller, M.L., Dutang, C., 2015. *Fittistrplus: an R Package for fitting distributions*. *J. Stat. Softw.* 64, 1–34.
- Dioguardi, F., Mele, D., Dellino, P., Dürig, T., 2017. The terminal velocity of volcanic particles with shape obtained from 3D X-ray microtomography. *J. Volcanol. Geotherm. Res.* 329, 41–53. <https://doi.org/10.1016/j.jvolgeores.2016.11.013>.
- Dugmore, A.J., Newton, A.J., 1992. Thin tephra layers in peat revealed by X-radiography. *J. Archaeol. Sci.* 19, 163–170. [https://doi.org/10.1016/0305-4403\(92\)90047-7](https://doi.org/10.1016/0305-4403(92)90047-7).
- Durant, A.J., Shaw, R.A., Rose, W.I., Mi, Y., Ernst, G.G.J., 2008. Ice nucleation and overseeding of ice in volcanic clouds. *J. Geophys. Res.-Atmos.* 113. <https://doi.org/10.1029/2007JD009064>.
- Durant, A.J., Rose, W.I., Sarna-Wojcicki, A.M., Carey, S., Volentik, A.C.M., 2009. Hydrometeor-enhanced tephra sedimentation: Constraints from the 18 May 1980 eruption of Mount St. Helens. *J. Geophys. Res. Solid Earth* 114. <https://doi.org/10.1029/2008JB005756>.
- Dürig, T., White, J.D.L., Zimanowski, B., Büttner, R., Murch, A., Carey, R.J., 2020. Deep-sea fragmentation style of Havre revealed by dendrogrammatic analyses of particle morphometry. *Bull. Volcanol.* 82, 67. <https://doi.org/10.1007/s00445-020-01408-1>.
- Engwell, S.L., Eychenne, J., 2016. Contribution of fine ash to the atmosphere from plumes associated with pyroclastic density currents. *Volcanic Ash: Hazard Observation*. Elsevier, pp. 67–85.
- Engwell, S.L., Sparks, R.S.J., Carey, S., 2014. Physical characteristics of tephra layers in the deep sea realm: the Campanian Ignimbrite eruption. *Geol. Soc. Lond. Spec. Publ.* 398, 47–64. <https://doi.org/10.1144/SP398.7>.
- Eychenne, J., Le Pennec, J.-L., Troncoso, L., Gouhier, M., Nedelec, J.-M., 2012. Causes and consequences of bimodal grain-size distribution of tephra fall deposited during the August 2006 Tungurahua eruption (Ecuador). *Bull. Volcanol.* 74, 187–205. <https://doi.org/10.1007/s00445-011-0517-5>.
- Eychenne, J., Cashman, K., Rust, A., Durant, A., 2015. Impact of the lateral blast on the spatial pattern and grain size characteristics of the 18 May 1980 Mount St. Helens fallout deposit. *J. Geophys. Res. Solid Earth* 120, 6018–6038. <https://doi.org/10.1002/2015JB012116>.
- Fairbridge, R.W., Bourgeois Joanne, 1978. The Encyclopedia of sedimentology, Encyclopedia of earth sciences series ; v. 6. Dowden, Hutchinson & Ross ;, Stroudsburg, Pa.
- Fenner, C.N., 1937. Tufts and other volcanic deposits at Katmai and Yellowstone Park. *EOS Trans. Am. Geophys. Union* 18, 236–239. <https://doi.org/10.1029/TR018i001p00236>.
- Fierstein, J., Nathenson, M., 1992. Another look at the calculation of fallout tephra volumes. *Bull. Volcanol.* 54, 156–167. <https://doi.org/10.1007/BF00278005>.
- Figueiredo, M.M., 2006. Electrozone sensing in particle size analysis, in: encyclopedia of analytical chemistry. Am. Cancer Soc. <https://doi.org/10.1002/9780470027318.a1504>.
- Fisher, R.V., 1964. Maximum size, median diameter, and sorting of tephra. *J. Geophys. Res.* 1896–1977 (69), 341–355. <https://doi.org/10.1029/JZ069i002p00341>.
- Folk, R.L., Ward, W.C., 1957. Brazos River bar [Texas]: a study in the significance of grain size parameters. *J. Sediment. Res.* 27, 3–26. <https://doi.org/10.1306/74D70646-2B21-11D7-8648000102C1865D>.
- Freret-Lorgeril, V., Donnadieu, F., Eychenne, J., Soriaux, C., Latchimy, T., 2019. In situ terminal settling velocity measurements at Stromboli volcano: Input from physical characterization of ash. *J. Volcanol. Geotherm. Res.* 374, 62–79. <https://doi.org/10.1016/j.jvolgeores.2019.02.005>.
- Ganser, G.H., 1993. A rational approach to drag prediction of spherical and nonspherical particles. *Powder Technol.* 77, 143–152.
- Genareau, K., Wallace, K.L., Gharghab, P., Gafford, J., 2019. Lightning Effects on the grain size distribution of Volcanic Ash. *Geophys. Res. Lett.* 46, 3133–3141. <https://doi.org/10.1029/2018GL081298>.
- Gibbs, R.J., Matthews, M.D., Link, D.A., 1971. The relationship between sphere size and settling velocity. *J. Sediment. Res.* 41, 7–18. <https://doi.org/10.1306/74D721D0-2B21-11D7-8648000102C1865D>.
- Gibbs, A., Charman, M., Schwarzscher, W., Rust, A.C., 2015. Immersion freezing of supercooled water drops containing glassy volcanic ash particles. *GeoResJ* 7, 66–69. <https://doi.org/10.1016/j.grj.2015.06.002>.
- Gouhier, M., Eychenne, J., Azzaoui, N., Guillain, A., Deslandes, M., Poret, M., Costa, A., Husson, P., 2019. Low efficiency of large volcanic eruptions in transporting very fine ash into the atmosphere. *Sci. Rep.* 9, 1–12. <https://doi.org/10.1038/s41598-019-3859-7>.
- Hadley, D., Hufford, G.L., Simpson, J.J., 2004. Resuspension of relic volcanic ash and dust from Katmai: still an aviation hazard. *Weather Forecast.* 19, 829–840. [https://doi.org/10.1175/1520-0434\(2004\)019<0829:RORVAA>2.0.CO;2](https://doi.org/10.1175/1520-0434(2004)019<0829:RORVAA>2.0.CO;2).
- Hails, J.R., Thompson, B.S., Cummings, L., 1973. An appraisal of the significance of sieve intervals in grain size analysis for environmental interpretation. *J. Sediment. Res.* 43.
- Heiken, G., 1972. Morphology and petrography of **volcanic ashes**. *GSA Bull.* 83, 1961–1988. [https://doi.org/10.1130/0016-7606\(1972\)83\[1961:MAPOVA\]2.0.CO;2](https://doi.org/10.1130/0016-7606(1972)83[1961:MAPOVA]2.0.CO;2).
- Hobbs, P.V., Radke, L.F., Lyons, J.H., Ferek, R.J., Coffman, D.J., Casadevall, T.J., 1991. Airborne measurements of particle and gas emissions from the 1990 volcanic eruptions of Mount Redoubt. *J. Geophys. Res.-Atmos.* 96, 18735–18752. <https://doi.org/10.1029/91JD01635>.
- Horwell, C., 2007. Grain-size analysis of volcanic ash for the rapid assessment of respiratory health hazard. *J. Environ. Monit.* 9, 1107–1115. <https://doi.org/10.1039/B710583P>.
- Horwell, C.J., Baxter, P.J., 2006. The respiratory health hazards of volcanic ash: a review for volcanic risk mitigation. *Bull. Volcanol.* 69, 1–24. <https://doi.org/10.1007/s00445-006-0052-y>.
- Horwell, C.J., Sparks, R.S.J., Brewer, T.S., Llewellyn, E.W., Williamson, B.J., 2003. Characterization of respirable volcanic ash from the Soufrière Hills volcano, Montserrat, with implications for human health hazards. *Bull. Volcanol.* 65, 346–362. <https://doi.org/10.1007/s00445-002-0266-6>.
- Inman, D.L., 1952. Measures for describing the size distribution of sediments. *J. Sediment. Res.* 22, 125–145. <https://doi.org/10.1306/D42694DB-2B26-11D7-8648000102C1865D>.
- James, M.R., Lane, S.J., Gilbert, J.S., 2000. Volcanic plume electrification: Experimental investigation of a fracture-charging mechanism. *J. Geophys. Res. Solid Earth* 105, 16641–16649. <https://doi.org/10.1029/2000JB000068>.
- Johnson, B., Turnbull, K., Brown, P., Burgess, R., Dorsey, J., Baran, A.J., Webster, H., Haywood, J., Cotton, R., Ulanowski, Z., 2012. *In situ observations of volcanic ash clouds from the FAAM aircraft during the eruption of Eyjafjallajökull in 2010*. *J. Geophys. Res.-Atmos.* 117.
- Jones, T.J., McNamara, K., Eychenne, J., Rust, A.C., Cashman, K.V., Scheu, B., Edwards, R., 2016. Primary and secondary fragmentation of crystal-bearing intermediate magma. *J. Volcanol. Geotherm. Res.* 327, 70–83. <https://doi.org/10.1016/j.jvolgeores.2016.06.022>.
- Jonkers, L., Prins, M.A., Brummer, G.-J.A., Konert, M., Lougheed, B.C., 2009. Experimental insights into laser diffraction particle sizing of fine-grained sediments for use in palaeoceanography. *Sedimentology* 56, 2192–2206. <https://doi.org/10.1111/j.1365-3091.2009.01076.x>.
- Jutzeler, M., Proussevitch, A.A., Allen, S.R., 2012. Grain-size distribution of volcanoclastic rocks 1: a new technique based on functional stereology. *J. Volcanol. Geotherm. Res.* 239–240, 1–11. <https://doi.org/10.1016/j.jvolgeores.2012.05.013>.
- Komar, P.D., Cui, B., 1984. The analysis of grain-size measurements by sieving and settling-tube techniques. *J. Sediment. Res.* 54, 603–614. <https://doi.org/10.1306/212F8481-2B24-11D7-8648000102C1865D>.
- Koyaguchi, T., Ohno, M., 2001. Reconstruction of eruption column dynamics on the basis of grain size of tephra fall deposits: 1. Methods. *J. Geophys. Res.: Solid Earth* 106, 6499–6512. <https://doi.org/10.1029/2000JB000426>.
- Kozono, T., Iguchi, M., Miwa, T., Maki, M., Maesaka, T., Miki, D., 2019. Characteristics of tephra fall from eruptions at Sakurajima volcano, revealed by optical disrometer measurements. *Bull. Volcanol.* 81, 41. <https://doi.org/10.1007/s00445-019-1300-2>.
- Krumbein, W.C., 1934. Size frequency distributions of sediments. *J. Sediment. Res.* 4, 65–77. <https://doi.org/10.1306/D4268EB9-2B26-11D7-8648000102C1865D>.
- Kylling, A., Kahnert, M., Lindqvist, H., Nousiainen, T., 2014. Volcanic ash infrared signature: porous non-spherical ash particle shapes compared to homogeneous spherical ash particles. *Atmosph. Meas. Techniq.* 7, 919–929. <https://doi.org/10.5194/amt-7-919-2014>.
- Lacroix, A., 1904. *La Montagne Pelée et ses éruptions*. Masson.
- Leadbetter, S., Hort, M., Löwis, S., Weber, K., Witham, C., 2012. Modeling the resuspension of ash deposited during the eruption of Eyjafjallajökull in spring 2010. *J. Geophys. Res.-Atmos.* 117.
- Leibrandt, S., Le Pennec, J.-L., 2015. Towards fast and routine analyses of volcanic ash morphology for eruption surveillance applications. *J. Volcanol. Geotherm. Res.* 297, 11–27. <https://doi.org/10.1016/j.jvolgeores.2015.03.014>.
- Liu, E.J., Cashman, K.V., Beckett, F.M., Witham, C.S., Leadbetter, S.J., Hort, M.C., Guhmundsson, S., 2014. Ash mists and brown snow: Remobilization of volcanic ash from recent Icelandic eruptions. *J. Geophys. Res.-Atmos.* 119, 9463–9480. <https://doi.org/10.1002/2014JD021598>.
- Liu, E.J., Cashman, K.V., Rust, A.C., 2015. Optimising shape analysis to quantify volcanic ash morphology. *GeoResJ* 8, 14–30.
- Liu, E.J., Cashman, K.V., Rust, A.C., Höskuldsson, A., 2017. Contrasting mechanisms of magma fragmentation during coeval magmatic and hydromagmatic activity: the

- Hverfjall Fires fissure eruption, Iceland. *Bull. Volcanol.* 79, 68. <https://doi.org/10.1007/s00445-017-1150-8>.
- Macias Garcia, A., Cuerda Correa, E.M., Diaz Diez, M.A., 2004. Application of the Rosin-Rammler and Gates-Gaudin-Schuhmann models to the particle size distribution analysis of agglomerated cork. *Mater. Charact.* 52, 159–164. <https://doi.org/10.1016/j.matchar.2004.04.007>.
- Mastin, L.G., Guffanti, M., Servranckx, R., Webley, P., Barsotti, S., Dean, K., Durant, A., Ewert, J.W., Neri, A., Rose, W.I., 2009. A multidisciplinary effort to assign realistic source parameters to models of volcanic ash-cloud transport and dispersion during eruptions. *J. Volcanol. Geotherm. Res.* 186, 10–21.
- McNamara, K., Cashman, K.V., Rust, A.C., Fontijn, K., Chalié, F., Tomlinson, E.L., Yirgu, G., 2018. Using Lake Sediment Cores to Improve Records of Volcanism at Aluto Volcano in the Main Ethiopian Rift. *Geochem. Geophys. Geosyst.* 19, 3164–3188. <https://doi.org/10.1029/2018GC007686>.
- Mele, D., Dellino, P., Sulpizio, R., Braia, G., 2011. A systematic investigation on the aerodynamics of ash particles. *J. Volcanol. Geotherm. Res.* 203, 1–11. <https://doi.org/10.1016/j.jvolgeores.2011.04.004>.
- Mele, D., Costa, A., Dellino, P., Sulpizio, R., Dioguardi, F., Isaia, R., Macedonio, G., 2020. Total grain size distribution of components of fallout deposits and implications for magma fragmentation mechanisms: examples from Campi Flegrei caldera (Italy). *Bull. Volcanol.* 82, 31. <https://doi.org/10.1007/s00445-020-1368-8>.
- Meredith, P., 2019. Using the May 18, 1980 ash fallout deposit of Mount Saint Helens to compare methods of particle size analysis (Masters Thesis). University of Bristol.
- Microtrac MRB, 2020. CAMSIZER X2 - Particle Size & Shape Analyzer - Microtrac [WWW Document]. MicroTrac MRB <https://www.microtrac.com/products/particle-size-shape-analysis/dynamic-image-analysis/camsizer-x2/function-features> accessed 3.26.20).
- Miffre, A., David, G., Thomas, B., Rairoux, P., Fjaeraa, A.M., Kristiansen, N.I., Stohl, A., 2012. Volcanic aerosol optical properties and phase partitioning behavior after long-range advection characterized by UV-Lidar measurements. Atmospheric Environment, Volcanic ash over Europe during the eruption of Eyjafjallajökull on Iceland, April–May 2010. 48, pp. 76–84. <https://doi.org/10.1016/j.atmosenv.2011.03.057>.
- Miura, T., Koyaguchi, T., Tanaka, Y., 2002. Measurements of electric charge distribution in volcanic plumes at Sakurajima Volcano, Japan. *Bull. Volcanol.* 64, 75–93. <https://doi.org/10.1007/s00445-001-0182-1>.
- Miwa, T., Iriyama, Y., Nagai, M., Nanayama, F., 2020. Sedimentation process of ashfall during a Vulcanian eruption as revealed by high-temporal-resolution grain size analysis and high-speed camera imaging. *Progress in Earth and Planet. Sci.* 7, 3. <https://doi.org/10.1186/s40645-019-0316-8>.
- Moore, B.N., 1934. Deposits of possible Nuée Ardente Origin in the Crater Lake Region, Oregon. *J. Geol.* 42, 358–375. <https://doi.org/10.1086/624174>.
- Mori, T., Hashimoto, T., Terada, A., Yoshimoto, M., Kazahaya, R., Shinohara, H., Tanaka, R., 2016. Volcanic plume measurements using a UAV for the 2014 Mt. Ontake eruption. *Earth, Planets and Space* 68, 49. <https://doi.org/10.1186/s40623-016-0418-0>.
- Muñoz, O., Volten, H., Hovenier, J.W., Veihelmann, B., van der Zande, W.J., Waters, L.B.F.M., Rose, W.I., 2004. Scattering matrices of volcanic ash particles of Mount St. Helens, Redoubt, and Mount Spurr Volcanoes. *J. Geophys. Res.-Atmos.* 109. <https://doi.org/10.1029/2004JD004684>.
- OTT, 2020. OTT Parsivel2 - Laser Weather Sensor [WWW Document]. OTT Hydromet <https://www.ott.com/download/operating-instructions-present-weather-sensor-ott-parsivel2-without-screen-heating-1> accessed 12.3.20).
- Palais, J.M., Germani, M.S., Zieliński, G.A., 1992. Inter-hemispheric Transport of Volcanic Ash from a 1259 A.D. Volcanic Eruption to the Greenland and Antarctic Ice Sheets. *Geophys. Res. Lett.* 19, 801–804. <https://doi.org/10.1029/92GL00240>.
- Panalytical, Malvern, 2020. Mastersizer 3000 | World's Leading Particle Size Analyzer | Malvern Panalytical [WWW Document]. Malvern Panalytical <https://www.malvernpanalytical.com/en/products/product-range/mastersizer-range/mastersizer-3000> accessed 4.27.20).
- Panebianco, J.E., Mendez, M.J., Buschiazzo, D.E., Bran, D., Gaitán, J.J., 2017. Dynamics of volcanic ash remobilisation by wind through the Patagonian steppe after the eruption of Córdón Caulle, 2011. *Sci. Rep.* 7, 45529. <https://doi.org/10.1038/srep45529>.
- Pavolonis, M.J., Heidinger, A.K., Sieglaff, J., 2013. Automated retrievals of volcanic ash and dust cloud properties from upwelling infrared measurements. *J. Geophys. Res.-Atmos.* 118, 1436–1458. <https://doi.org/10.1002/jgrd.50173>.
- Petäjä, T., Laakso, L., Grönholm, T., Launiainen, S., Evele-Peltoniemi, I., Virkkula, A., Leskinen, A., Backman, J., Manninen, H.E., Sipilä, M., Haapanala, S., Hämeri, K., Vanhala, E., Tuomi, T., Paatero, J., Aurela, M., Hakola, H., Makkonen, U., Hellén, H., Hillamo, R., Vira, J., Prank, M., Sofiev, M., Siitari-Kauppi, M., Laaksonen, A., Lehtinen, K.E.J., Kulmala, M., Viisanen, Y., Kerminen, V.-M., 2012. In-situ observations of Eyjafjallajökull ash particles by hot-air balloon. Atmospheric Environment. Volcanic ash over Europe during the eruption of Eyjafjallajökull on Iceland, April–May 2010. 48, pp. 104–112. <https://doi.org/10.1016/j.atmosenv.2011.08.046>.
- Pettijohn, F.J., 1949. *Sedimentary Rocks* (Harper & Row New York).
- Pieri, D., Ma, C., Simpson, J.J., Hufford, G., Grindle, T., Grove, C., 2002. Analyses of in-situ airborne volcanic ash from the February 2000 eruption of Hekla Volcano, Iceland. *Geophys. Res. Lett.* 29. <https://doi.org/10.1029/2001GL013688> 19-1–19–4.
- Pioli, L., Bonadonna, C., Pistolesi, M., 2019. Reliability of total grain-size distribution of tephra deposits. *Sci. Rep.* 9, 10006. <https://doi.org/10.1038/s41598-019-46125-8>.
- Prata, A.J., 1989. Infrared radiative transfer calculations for volcanic ash clouds. *Geophys. Res. Lett.* 16, 1293–1296. <https://doi.org/10.1029/GL016i011p01293>.
- Prata, A.J., Grant, I.F., 2001. Retrieval of microphysical and morphological properties of volcanic ash plumes from satellite data: Application to Mt Ruapehu, New Zealand. *Q. J. R. Meteorol. Soc.* 127, 2153–2179. <https://doi.org/10.1002/qj.49712757615>.
- Prata, A.J., Prata, A.T., 2012. Eyjafjallajökull volcanic ash concentrations determined using Spin Enhanced Visible and Infrared Imager measurements. *J. Geophys. Res.-Atmos.* 117 <https://doi.org/10.1029/2011JD016800>.
- Pyle, D.M., 1989. The thickness, volume and grainsize of tephra fall deposits. *Bull. Volcanol.* 51, 1–15.
- Rampino, M.R., Self, S., 1993. Climate-Volcanism Feedback and the Toba Eruption of ~74,000 years Ago. *Quat. Res.* 40, 269–280. <https://doi.org/10.1006/qres.1993.1081>.
- Riley, C.M., Rose, W.I., Bluth, G.J.S., 2003. Quantitative shape measurements of distal volcanic ash. *J. Geophys. Res. Solid Earth* 108. <https://doi.org/10.1029/2001JB000818>.
- Roller, P.S., 1931. *Separation and Size Distribution of Microscopic Particles: An Air Analyzer for Fine Powders*. U.S. Government Printing Office.
- Román-Sierra, J., Muñoz-perez, J.J., Navarro-Pons, M., 2013. Influence of sieving time on the efficiency and accuracy of grain-size analysis of beach and dune sands. *Sedimentology* 60, 1484–1497. <https://doi.org/10.1111/sed.12040>.
- Rose, W.I., Durant, A.J., 2009. Fine ash content of explosive eruptions. *J. Volcanol. Geothermal Research*, Improved Prediction and Tracking of Volcanic Ash Clouds 186, 32–39. <https://doi.org/10.1016/j.jvolgeores.2009.01.010>.
- Rosin, P., Rammler, E., 1933. The laws governing the finesness of powdered coal. *J. Inst. Fuel* 7, 29–36.
- Rossi, E., Bonadonna, C., Degruyter, W., 2019. A new strategy for the estimation of plume height from clast dispersal in various atmospheric and eruptive conditions. *Earth Planet. Sci. Lett.* 505, 1–12. <https://doi.org/10.1016/j.epsl.2018.10.007>.
- Sahagian, D.L., Proussevitch, A.A., 1998. 3D particle size distributions from 2D observations: stereology for natural applications. *J. Volcanol. Geotherm. Res.* 84, 173–196. [https://doi.org/10.1016/S0377-0273\(98\)00043-2](https://doi.org/10.1016/S0377-0273(98)00043-2).
- Sanford, R.B., Swift, D.J.P., 1971. Comparison of Sieving and Settling Techniques for size Analysis, using a Benthos Rapid Sediment Analyzer. *Sedimentology* 17, 257–264. <https://doi.org/10.1111/j.1365-3091.1971.tb01778.x>.
- Sarna-Wojciechski, A.M., Shipley, S., Waitt Jr., R.B., Dzurisin, D., Wood, S.H., 1981. Areal distribution, thickness, mass, volume, and grain size of air-fall ash from the six major eruptions of 1980. *US Geol. Surv. Prof. Pap.* 1250, 577–600.
- Sarocchi, D., Sulpizio, R., Macías, J.L., Saucedo, R., 2011. The 17 July 1999 block-and-ash flow (BAF) at Colima Volcano: New insights on volcanic granular flows from textural analysis. *J. Volcanol. Geotherm. Res.* 204, 40–56. <https://doi.org/10.1016/j.jvolgeores.2011.04.013>.
- Saxby, J., Beckett, F., Cashman, K., Rust, A., Tennant, E., 2018. The impact of particle shape on fall velocity: Implications for volcanic ash dispersion modelling. *J. Volcanol. Geotherm. Res.* 362, 32–48. <https://doi.org/10.1016/j.jvolgeores.2018.08.006>.
- Saxby, J., Rust, A., Cashman, K., Beckett, F., 2019. The importance of grain size and shape in controlling the dispersion of the Vedde cryptotephra. *J. Quater. Sci. Special Issue: Intav Tephra* <https://doi.org/10.1002/jqs.3152>.
- Saxby, J., Rust, A., Beckett, F., Cashman, K., Rodger, H., 2020. Estimating the 3D shape of volcanic ash to better understand sedimentation processes and improve atmospheric dispersion modelling. *Earth Planet. Sci. Lett.* 534, 116075. <https://doi.org/10.1016/j.epsl.2020.116075>.
- Scarpati, C., Sparice, D., Perrotta, A., 2014. A crystal concentration method for calculating ignimbrite volume from distal ash-fall deposits and a reappraisal of the magnitude of the Campanian Ignimbrite. *J. Volcanol. Geotherm. Res.* 280, 67–75. <https://doi.org/10.1016/j.jvolgeores.2014.05.009>.
- Schellenberg, B., Richardson, T., Watson, M., Greatwood, C., Clarke, R., Thomas, R., Wood, K., Freer, J., Thomas, H., Liu, E., Salama, F., Chigna, G., 2019. Remote sensing and identification of volcanic plumes using fixed-wing UAVs over Volcán de Fuego, Guatemala. *J. Field Robotics* 36, 1192–1211. <https://doi.org/10.1002/rob.21896>.
- Scollo, S., Coltellini, M., Prodi, F., Folegani, M., Natali, S., 2005. Terminal settling velocity measurements of volcanic ash during the 2002–2003 Etna eruption by an X-band microwave rain gauge disdrometer. *Geophys. Res. Lett.* 32. <https://doi.org/10.1029/2004GL022100>.
- Sheridan, M.F., 1971. Particle-size characteristics of Pyroclastic Tuffs. *J. Geophys. Res.* 1896–1977 (76), 5627–5634. <https://doi.org/10.1029/B076i023p05627>.
- Sparks, R.S.J., 1976. Grain size variations in ignimbrites and implications for the transport of pyroclastic flows. *Sedimentology* 23, 147–188. <https://doi.org/10.1111/j.1365-3091.1976.tb00045.x>.
- Sparks, R.S.J., Walker, G.P.L., 1977. The significance of vitric-enriched air-fall ashes associated with crystal-enriched ignimbrites. *J. Volcanol. Geotherm. Res.* 2, 329–341. [https://doi.org/10.1016/0377-0273\(77\)90019-1](https://doi.org/10.1016/0377-0273(77)90019-1).
- Sparks, R.S.J., Brazier, S., Huang, T.C., Muerdter, D., 1983. Sedimentology of the Minoan deep-sea tephra layer in the Aegean and Eastern Mediterranean. *Mar. Geol.* 54, 131–167. [https://doi.org/10.1016/0025-3227\(83\)90011-7](https://doi.org/10.1016/0025-3227(83)90011-7).
- Sparks, R.S.J., Bursik, M.I., Ablay, G.J., Thomas, R.M.E., Carey, S.N., 1992. Sedimentation of tephra by volcanic plumes. Part 2: controls on thickness and grain-size variations of tephra fall deposits | SpringerLink. *Bull. Volcanol.* 54, 685–695. <https://doi.org/10.1007/BF00430779>.
- Stevenson, J.A., Millington, S.C., Beckett, F.M., Swindles, G.T., Thordarson, T., 2015. Big grains go far: understanding the discrepancy between tephrochronology and satellite infrared measurements of volcanic ash. *Atmosph. Measurement Techniq.* 8, 2069–2091. <https://doi.org/10.5194/amt-8-2069-2015>.
- Swineford, A., Swineford, F., 1946. A comparison of three sieve shakers. *J. Sediment. Res.* 16, 3–13. <https://doi.org/10.1306/D426923D-2B26-11D7-8648000102C1865D>.
- Visher, G.S., 1969. Grain size distributions and depositional processes. *J. Sediment. Res.* 39, 1074–1106.
- Vonlanthen, P., Rausch, J., Ketcham, R.A., Putlitz, B., Baumgartner, L.P., Grobety, B., 2015. High-resolution 3D analyses of the shape and internal constituents of small volcanic ash particles: the contribution of SEM micro-computed tomography (SEM micro-CT). *J. Volcanol. Geotherm. Res.* 293, 1–12. <https://doi.org/10.1016/j.jvolgeores.2014.11.016>.
- Vriend, M., Prins, M.A., 2005. Calibration of modelled mixing patterns in loess grain-size distributions: an example from the north-eastern margin of the Tibetan Plateau, China. *Sedimentology* 52, 1361–1374. <https://doi.org/10.1111/j.1365-3091.2005.00743.x>.

- Walker, G.P.L., 1971. Grain-size Characteristics of Pyroclastic Deposits. *J. Geol.* 79, 696–714. <https://doi.org/10.1086/627699>.
- Walker, G.P.L., 1980. The Taupo pumice: product of the most powerful known (ultraplinian) eruption? *J. Volcanol. Geotherm. Res.* 8, 69–94. [https://doi.org/10.1016/0377-0273\(80\)90008-6](https://doi.org/10.1016/0377-0273(80)90008-6).
- Walker, G.P.L., 1981. The Waimihia and Hatepe Plinian deposits from the rhyolitic Taupo Volcanic Centre. *N. Z. J. Geol. Geophys.* 24, 305–324. <https://doi.org/10.1080/00288306.1981.10422722>.
- Watanabe, K., Ono, K., Sakaguchi, K., Takada, A., Hoshizumi, H., 1999. Co-ignimbrite ash-fall deposits of the 1991 eruptions of Fugen-dake, Unzen Volcano, Japan. *J. Volcanol. Geotherm. Res.* 89, 95–112. [https://doi.org/10.1016/S0377-0273\(98\)00126-7](https://doi.org/10.1016/S0377-0273(98)00126-7).
- Webley, P.W., Stunder, B.J.B., Dean, K.G., 2009. Preliminary sensitivity study of eruption source parameters for operational volcanic ash cloud transport and dispersion models—a case study of the August 1992 eruption of the Crater Peak vent, Mount Spurr, Alaska. *J. Volcanol. Geotherm. Res.* 186, 108–119.
- Weibull, W., 1951. A statistical distribution function of wide applicability. *J. Appl. Mech. Transac. Am. Soc. Mech. Eng.* 293–297.
- Wen, S., Rose, W.I., 1994. Retrieval of sizes and total masses of particles in volcanic clouds using AVHRR bands 4 and 5. *J. Geophys. Res.-Atmos.* 99, 5421–5431. <https://doi.org/10.1029/93JD03340>.
- Wentworth, C.K., 1922. A scale of grade and class terms for clastic sediments. *J. Geol.* 30, 377–392.
- Wiesner, M.G., Wetzel, A., Catane, S.G., Listanco, E.L., Mirabueno, H.T., 2004. Grain size, areal thickness distribution and controls on sedimentation of the 1991 Mount Pinatubo tephra layer in the South China Sea. *Bull. Volcanol.* 66, 226–242. <https://doi.org/10.1007/s00445-003-0306-x>.
- Williams, S.N., Self, S., 1983. The October 1902 Plinian eruption of Santa Maria volcano, Guatemala. *J. Volcanol. Geotherm. Res.* 16, 33–56. [https://doi.org/10.1016/0377-0273\(83\)90083-5](https://doi.org/10.1016/0377-0273(83)90083-5).
- Wilson, L., Huang, T.C., 1979. The influence of shape on the atmospheric settling velocity of volcanic ash particles. *Earth Planet. Sci. Lett.* 44, 311–324. [https://doi.org/10.1016/0012-821X\(79\)90179-1](https://doi.org/10.1016/0012-821X(79)90179-1).
- Wilson, T.M., Stewart, C., Sword-Daniels, V., Leonard, G.S., Johnston, D.M., Cole, J.W., Wardman, J., Wilson, G., Barnard, S.T., 2012. *Volcanic ash impacts on critical infrastructure*. Phys. Chem. Earth, Parts A/B/C 45, 5–23.
- WMO, 2018. VAAC Operational Dispersion Model Configuration Snap Shot Version 3 (No. 3), VAAC Best Practice process for the VAAC 'Inputs and Outputs' Modelling Workshop held at NCEP, Washington 2012.
- Wohletz, K.H., Sheridan, M.F., Brown, W.K., 1989. Particle size distributions and the sequential fragmentation/transport theory applied to volcanic ash. *J. Geophys. Res. Solid Earth* 94, 15703–15721. <https://doi.org/10.1029/JB094iB11p15703>.
- Woods, A.W., Wohletz, K., 1991. Dimensions and dynamics of co-ignimbrite eruption columns. *Nature* 350, 225.
- Young, S.R., 1990. *Physical volcanology of Holocene airfall deposits from Mt Mazama, Crater Lake, Oregon*. (PhD Thesis). University of Lancaster.
- Yu, Y., 2018. mixR: Finite Mixture Modeling for Raw and Binned Data.
- Zdanowicz, C., Zielinski, G., Germani, M., 1999. Mount Mazama eruption: Calendrical age verified and atmospheric impact assessed. *GEOLOGY* 27, 621–624. [https://doi.org/10.1130/0091-7613\(1999\)027<0621:MMECAV>2.3.CO;2](https://doi.org/10.1130/0091-7613(1999)027<0621:MMECAV>2.3.CO;2).